

# POST-IRRADIATION EXAMINATION OF HFIR-IRRADIATED YTTRIUM HYDRIDES



M Nedim Cinbiz  
Annabelle Le Coq  
Shaileyee Bhattacharya  
Mobashera Saima Haque  
Yan-Ru Lin  
David Sprouster  
Kory Linton

**September 2025**



## DOCUMENT AVAILABILITY

**Online Access:** US Department of Energy (DOE) reports produced after 1991 and a growing number of pre-1991 documents are available free via <https://www.osti.gov>.

The public may also search the National Technical Information Service's [National Technical Reports Library \(NTRL\)](#) for reports not available in digital format.

DOE and DOE contractors should contact DOE's Office of Scientific and Technical Information (OSTI) for reports not currently available in digital format:

US Department of Energy  
Office of Scientific and Technical Information  
PO Box 62  
Oak Ridge, TN 37831-0062  
**Telephone:** (865) 576-8401  
**Fax:** (865) 576-5728  
**Email:** [reports@osti.gov](mailto:reports@osti.gov)  
**Website:** [www.osti.gov](http://www.osti.gov)

This report was prepared as an account of work sponsored by an agency of the United States Government. Neither the United States Government nor any agency thereof, nor any of their employees, makes any warranty, express or implied, or assumes any legal liability or responsibility for the accuracy, completeness, or usefulness of any information, apparatus, product, or process disclosed, or represents that its use would not infringe privately owned rights. Reference herein to any specific commercial product, process, or service by trade name, trademark, manufacturer, or otherwise, does not necessarily constitute or imply its endorsement, recommendation, or favoring by the United States Government or any agency thereof. The views and opinions of authors expressed herein do not necessarily state or reflect those of the United States Government or any agency thereof.

Materials Science and Technology Division

**POST-IRRADIATION EXAMINATION OF HFIR-IRRADIATED YTTRIUM  
HYDRIDES**

M Nedim Cinbiz  
Annabelle Le Coq  
Shaileyee Bhattacharya  
Yan-Ru Lin  
David Sprouster  
Kory Linton

September 2025

Prepared by  
OAK RIDGE NATIONAL LABORATORY  
Oak Ridge, TN 37831  
managed by  
UT-BATTELLE LLC  
for the  
US DEPARTMENT OF ENERGY  
under contract DE-AC05-00OR22725





## CONTENTS

1.	Introduction .....	1
2.	Summary of HFIR irradiations.....	2
3.	Post-irradiation examination plan .....	4
4.	Specimen inspection methods prior to irradiations .....	5
5.	Post-irradiation examination .....	6
5.1	SiC passive thermometry analysis.....	6
5.2	Thermal property measurements .....	6
5.3	TEM characterizations .....	8
5.4	High-energy through-thickness XRD measurements .....	9
6.	Results .....	11
6.1	SiC passive thermometry.....	11
6.2	Visual Examination .....	11
6.3	Dimensional change .....	17
6.4	Synchrotron XRD analysis .....	18
6.5	Microscopy results .....	22
6.6	Thermal property results .....	28
6.6.1	LFA results .....	28
6.6.2	DSC results.....	31
7.	Key discussions .....	38
7.1	Effect of local varying hydride and metal phase fraction on the H retention .....	38
7.2	Hydride stability under irradiation .....	39
7.3	Microstructure and H retention .....	40
7.4	Importance of an accurate hydrogen retention metric for irradiated specimens .....	40
8.	Conclusions and suggested future work .....	41
9.	References .....	42

## LIST OF FIGURES

Figure 2-1 Irradiation capsule design [6, 7, 14].....	3
Figure 2-2 Capsule parts layout (a) YHS01 and (b) YHS03 .....	3
Figure 2-3 Representative temperature distribution in $\text{YH}_x$ specimens for a capsule design targeting an irradiation temperature of 600°C. ....	4
Figure 4-1 Keyence images of specimen TY39 with recorded measurements of the engraved markings pre-irradiation. ....	6
Figure 5-1 Pictures of (a) DSC and (b) LFA equipment located at LAMDA .....	7
Figure 5-2 Depiction of transition temperature determination through finding local maximum and minimums. ....	8
Figure 5-3 TEM specimen preparation procedure, specimens were not ground or polished at the outer surface to characterize the near surface microstructure from the hydrogen retention perspective. ....	9
Figure 5-4 Schematic representation of synchrotron XRD experimental setup in transmission mode. The incident synchrotron beam passes through the sample, and the diffracted intensities are recorded by the XRD detector. ....	10
Figure 5-5 1D diffraction spectrum of reference $\text{LaB}_6$ powder sample. The inset shows the corresponding 2D diffraction pattern measured at 74.5 keV energy. ....	10
Figure 6-1 Predicted and experimental average specimen temperature for each $\text{YH}_x$ capsule.....	11
Figure 6-2 Dimensional change measured at 6 locations between engraved lines (depicted with a yellow line). Each data point is the dimensional change for an individual specimen. The average dimensional change relative to the pre-irradiation measurement at each location is plotted as a histogram with standard deviation of the measurement shown on the error bar. ....	18
Figure 6-3 Experimental XRD patterns of non-irradiated $\text{YH}_x$ specimens having different stoichiometries ranging from 1.52 to 1.90. ....	20
Figure 6-4 Changes in the peak intensities of $\alpha\text{-Y}$ and $\delta\text{-YH}_2$ due to stoichiometry of $\text{YH}_x$ specimens. The red dotted line is to guide the eye. ....	21
Figure 6-5 Experimental XRD patterns of irradiated $\text{YH}_x$ specimens in capsule YHS01.....	21
Figure 6-6 Experimental XRD patterns of irradiated $\text{YH}_x$ specimens in capsule YHS03.....	22
Figure 6-7 Microstructure near specimen periphery and diffraction patterns from the amorphous region.....	23
Figure 6-8 Thickness of the amorphous region with respect to neutron dose and irradiation temperature.....	24
Figure 6-9 STEM-ADF images and EDS maps of O distribution at the interface of amorphous and hydride regions for specimens of (a) 0.1 dpa, (b) 1 dpa, and (c) 2 dpa; (d) oxide layer thickness vs neutron dose .....	25
Figure 6-10 (a-c) STEM-ADF image and (d-f) EDS maps of near interface microstructure of specimens.....	25
Figure 6-11 STEM images and EDS Ca and F elemental maps of irradiated yttrium hydride specimens.....	26
Figure 6-12 $\text{CaF}_2$ precipitate density and diameter as a function of neutron dose .....	26
Figure 6-13 STEM-BF images showing dislocation loop microstructure in $\text{YH}_x$ matrix for different irradiation conditions .....	27
Figure 6-14 Dislocation loop density and diameter as a function of neutron dose.....	27

Figure 6-15 TEM under-focused images showing cavity microstructure in $\text{YH}_x$ matrix for different irradiation conditions .....	28
Figure 6-16 Cavity density and diameter as a function of neutron dose .....	28
Figure 6-17 Thermal diffusivity of specimens (as-fabricated H/Y ratio was 1.87) irradiated at 532°C up to 2 dpa. (TY63, TY66, and TY67 from capsule YHS01) .....	29
Figure 6-18 Thermal diffusivity of specimens (as-fabricated H/Y ratio was 1.87) irradiated at 597°C up to 2 dpa. (TY05, TY16, and TY50 from capsule YHS03) .....	30
Figure 6-19 Capsule averaged thermal diffusivity (a) YHS01 and (b) YHS03 .....	30
Figure 6-20 Specific heat capacity of specimen M013 (capsule YHXT07) for 2-cycle data collection. Initial H/Y ratio was 1.83, $T_{\text{irr}} = 616^\circ\text{C}$ , and 0.1 dpa. Inset shows the picture of the specimen. ....	32
Figure 6-21 Specific heat capacity of specimens from the capsule YHS01. In total 10 specimens were tested for 1-3 cycles. Initial H/Y ratio was 1.87, $T_{\text{irr}} = 532^\circ\text{C}$ , and 2 dpa. ....	33
Figure 6-22 Specific heat capacity of specimens from the capsule YHS03. In total 13 specimens were tested for 1-3 cycles. Initial H/Y ratio was 1.87, $T_{\text{irr}} = 597^\circ\text{C}$ , and 2 dpa. ....	34
Figure 6-23 Specific heat capacity of specimens from the capsules YHX08 ( $T_{\text{irr}} = 640^\circ\text{C}$ , 0.9 dpa) and YHX09 ( $T_{\text{irr}} = 532^\circ\text{C}$ , 2 dpa). Per capsule, 2 specimens were tested. Initial H/Y ratio of all specimens was 1.83 .....	35
Figure 6-24 Capsule averaged specific heat (a) YHS01 and (b) YHS03. The gray shaded region shows the $\pm 1\sigma$ bands .....	36
Figure 6-25 H/Y ratio versus transition temperatures, data is adapted and recalculated from [9, 22, 23] .....	37
Figure 7-1 Experimental XRD spectra obtained from different sampling locations within the same sample which has similar irradiation history as the specimens in capsules YHS01 and YHS03. The inset shows a schematic representation of the irradiated $\text{YH}_x$ disc, with different colored boxes representing the different probed volumes. The corresponding spectra obtained from each of these probed volumes are shown in the same color. The intensity ratio variations of $\{101\}$ diffraction peak of $\alpha\text{-Y}$ and $\{111\}$ $\delta\text{-YH}_2$ peak are indicated in the inset. ....	39
Figure 7-2 Illustration of H retention enhancing features in irradiated $\text{YH}_x$ .....	40

## LIST OF TABLES

Table 2-1 HFIR YH <sub>x</sub> irradiation test matrix (Campaign 1 and 2). .....	2
Table 3-1 Summary of the PIE .....	4
Table 6-1 Specimen list and pictures. For scale: diameter of a specimen is about 6 mm .....	12
Table 6-2: XRD peak intensity ratios of non-irradiated YH <sub>x</sub> specimens having different stoichiometries .....	20
Table 6-3 XRD peak intensity ratios of irradiated YH <sub>x</sub> specimens .....	22
Table 6-4 Capsule averaged thermal diffusivity of irradiated samples. <sup>1</sup> Calculation and <sup>2</sup> Measurement[10] .....	31
Table 6-5 Fit coefficients for 6 <sup>th</sup> degree polynomial for specific heat (only 1 <sup>st</sup> heating cycle data used). Mathematical form of the fit is: $c_p(T)=aT^6+ bT^5 +cT^4 +dT^3 +eT^2+fT+g$ .....	35
Table 6-6 H/Y ratio evolution and transition temperatures for YHS01 and YHS03 specimens .....	37

## Synonyms

ATR	Advanced Test Reactor
BNL	Brookhaven National Laboratory
C <sub>p</sub>	specific heat capacity
DSC	differential scanning calorimetry
dpa	displacements per atom
EDS	energy dispersive x-ray spectroscopy
FCC	face-centered cubic
FIB	focused ion beam
HFIR	High Flux Isotope Reactor
H/Y	hydrogen-to-yttrium atomic ratio
INL	Idaho National Laboratory
LAMDA	Low Activation Materials Development and Analysis facility
LFA	laser flash analysis
MRP	Microreactor program
NSLS-II	National Synchrotron Light Source II
ORNL	Oak Ridge National Laboratory
PIE	post-irradiation examination
PRF	permeation reduction factor
SEM	scanning electron microscope
SiC	silicon carbide
STEM	scanning transmission electron microscopy
TEM	transmission electron microscopy
TM	thermometry
TRL	technology readiness level
XRD	x-ray diffraction
YH <sub>x</sub>	yttrium hydride ( $x < 2$ )

## EXECUTIVE SUMMARY

The U.S. Department of Energy's Microreactor Program (MRP) is developing compact, high temperature microreactors requiring robust neutron moderators. Yttrium hydride ( $\text{YH}_x$ ), known for its high hydrogen retention and structural stability, is a leading candidate for this purpose. As part of ongoing evaluation, Oak Ridge National Laboratory (ORNL) conducted post-irradiation examinations (PIE) on  $\text{YH}_x$  specimens irradiated in the High Flux Isotope Reactor (HFIR) under the legacy Transformational Challenge Reactor program, focusing on their structural integrity, hydrogen retention, and thermal properties.

The PIE campaign primarily examined specimens from two irradiation campaigns, covering a range of hydrogen-to-yttrium (H/Y) ratios, neutron damage levels (0.1–2 dpa), and targeted irradiation temperature of 600 °C). The investigations included electron microscopy, high-energy X-ray diffraction (XRD), laser flash analysis (LFA), differential scanning calorimetry (DSC), and SiC thermometry analysis.

Key findings include:

- **Excellent hydrogen retention and structural stability:**  $\text{YH}_x$  maintained high structural integrity under irradiation, with minimal hydrogen loss.
- **Defect-driven H retention mechanisms:** Neutron irradiation induced dislocation loops, cavities, and amorphous-to-crystalline transitions that served as hydrogen storage, enhancing its retention. The formation of oxide and amorphous layers at interfaces further contributed to H retention.
- **Non-uniform hydrogen redistribution:** High-energy XRD revealed spatial variation in  $\text{YH}_x$  phase fraction, indicating non-uniform re-hydriding during reactor cool-down
- **Reliable H retention metric for irradiated specimens via thermal properties:** DSC-based order–disorder transition temperatures provided a robust, indirect method for estimating H/Y ratios post-irradiation, which can be scaled to larger specimens through dilatometry measurements in future
- **Thermal transport behavior:** Thermal diffusivity measurements followed a  $1/(A + BT)$  trend typical of phonon-dominated systems. Irradiated specimens showed higher A values (defect scattering) and slightly reduced B values (Umklapp scattering), supporting the link between irradiation-induced microstructure and thermal behavior.
- **Compatibility with dissimilar materials:**  $\text{YH}_x$  reacted with stainless steel and silicon carbide at contact points, but these interactions did not significantly degrade hydrogen retention.

To advance the technological readiness of hydride moderators, following future work is recommended:

- **Alloy development:** Leverage PIE findings to develop yttrium-based hydrides with superior hydrogen retention through microstructural control and compositional tuning.
- **Prototypic irradiation testing:** Advance to full-scale component irradiation to evaluate moderator-cladding systems under realistic operating conditions. HFIR provides a suitable platform for such work.
- **Integrated modeling and testing:** Combine computational modeling with experimental methods to explore new hydride materials and better understand hydrogen behavior under irradiation.

The results of this PIE campaign significantly advance the readiness of  $\text{YH}_x$  moderators for microreactor deployment and contribute critical data toward the development of next-generation nuclear moderator materials.

## **ACKNOWLEDGEMENTS**

This research is supported by the Microreactor program of the US Department of Energy (DOE), Office of Nuclear Energy. The report was authored by UT-Battelle under Contract No. DE-AC05-00OR22725 with the US DOE. Authors are grateful to Diane Li at the Department of Energy, John Jackson at INL, and Holly Treulleu at Los Alamos National Laboratory for their strong funding support of executing post-irradiation examination of HFIR-irradiated specimens at ORNL under DOE's Microreactor program. Lastly, we gladly acknowledge Kurt Terrani and Xunxiang Hu who have pioneered solid moderator studies at ORNL.



# POST-IRRADIATION EXAMINATION OF HFIR-IRRADIATED YTTRIUM HYDRIDES

## 1. INTRODUCTION

The U.S. Department of Energy's (DOE) Microreactor Program (MRP) is advancing key technologies to enable the deployment of truck-transportable, plug-and-play microreactors that operate at low power levels ( $< 20 \text{ MW}_{\text{th}}$ ), but at high temperatures ( $> 600 \text{ }^{\circ}\text{C}$ ), while ensuring inherently safe reactor operation [1, 2].

Due to the compact nature of microreactor cores, solid neutron moderators composed of light elements—such as hydrogen (H), carbon, or beryllium—are required. Among these, H-bearing materials with high hydrogen number density, particularly metal hydrides, are considered prime candidates[3-5]. Yttrium hydride ( $\text{YH}_x$ ,  $x < 2$ ) stands out due to its superior hydrogen retention capability and high-temperature structural stability. As a result, the DOE-MRP and the legacy Transformational Challenge Reactor (TCR) programs executed neutron irradiation campaigns at both the Advanced Test Reactor (ATR)[6, 7] and the High Flux Isotope Reactor (HFIR)[2], followed by post-irradiation examinations (PIE) at DOE national laboratory facilities.

The ATR irradiation campaign included various specimen geometries fabricated via powder metallurgy and direct hydriding methods, exposed to target temperatures of 600, 700, and 800  $^{\circ}\text{C}$  [2]. PIE activities were comprehensive and included neutron radiography, mass/volume/density measurements, hydrogen content determination, thermal property assessments—dilatometry, laser flash analysis (LFA), and differential scanning calorimetry (DSC)—laboratory X-ray diffraction (XRD), optical microscopy, and electron microscopy. Key findings from PIE conducted at INL included the observation of high structural stability of the hydrides, although hydrogen redistribution within the specimens was evident[8-10]. Dimensional and volumetric measurements were found to have low reliability, whereas thermal property data and laboratory XRD clearly demonstrated the dependence of thermal behavior on the H/Y ratio [8].

While the ATR irradiation testing and PIE have concluded in the Advanced Moderator handbook [11], PIE of HFIR-irradiated specimens aim to determine the essential physical and chemical properties of  $\text{YH}_x$  moderators, assess their structural stability, and establish operational limits in conjunction with proposed cladding materials [12, 13]. HFIR irradiations were conducted in two distinct campaigns. The first campaign focused on material property determination across a range of H/Y ratios (for target doses of 0.1, 1, and 2 dpa), with irradiation temperatures of 600 and 800  $^{\circ}\text{C}$ [12, 13]. The second campaign, by contrast, used a fixed H/Y ratio, dose, and temperature, and instead focused on hydride compatibility with dissimilar materials.

Information obtained from PIE of ATR-irradiated specimens helped establish key insights into hydride phase stability and hydrogen retention behavior[10]. Preliminary analyses of both INL and ORNL specimens suggested that microstructure plays a significant role in both hydrogen retention and thermal properties[12, 13]. ORNL's PIE activities included disassembly of irradiation vehicles, passive temperature verification, visual inspections, high-resolution electron microscopy, thermal property evaluation, and transmission-mode high-energy XRD. These examinations were primarily conducted on specimens from the second HFIR campaign, as they represented prototypic H/Y ratios and neutron dose levels at relevant irradiation temperatures.

This report presents a comprehensive description of the HFIR irradiation campaigns and initial specimen inspections, followed by the PIE activities and key findings. PIE was carried out at

ORNL's LAMDA facility, with high-energy XRD performed at the National Synchrotron Light Source II (NSLS-II) at Brookhaven National Laboratory (BNL). The results revealed new insights into hydrogen retention mechanisms in  $\text{YH}_x$ . Notably, second-campaign specimens exhibited excellent hydrogen retention at irradiation temperatures and projected end-of-life neutron doses. Furthermore, the findings suggest possible alloy development pathways for enhancing hydrogen retention. These results are discussed in the context of hydrogen behavior under irradiation, and recommendations for future work are outlined.

## 2. SUMMARY OF HFIR IRRADIATIONS

A total of 14 capsules were inserted in HFIR for irradiation testing. The corresponding irradiation test matrix is presented in Table 2-1. The YHXT capsules were part of the first irradiation campaign, aiming to neutron-irradiated  $\text{YH}_x$  specimens with 2 hydrogen contents, at an average irradiation temperature of approximately 600 and 900°C, and at irradiation damage levels of 0.1, 1, and 2 dpa [12]. The YHS capsules were part of a subsequent irradiation campaign, aiming to investigate the chemical compatibility of  $\text{YH}_x$  with silicon carbide (SiC) and stainless steel under irradiation at 600°C and 2 dpa.

Table 2-1 HFIR  $\text{YH}_x$  irradiation test matrix (Campaign 1 and 2).

Capsule ID	Fill gas composition (%He/Ar bal.)	Gas gap (μm)	H/Y	Irradiation damage (dpa)	Irradiation temperature (°C)	
					Calculated	Measured
YHXT01	100	189.5	1.69	0.1	596	595 ± 37
YHXT02	100	189.5	1.69	0.5	600	626 ± 2
YHXT13	97	170.5	1.69	2.0	602	663 ± 21
YHXT04	62	180.5	1.69	0.1	895	847 ± 14
YHXT05	62	180.5	1.69	0.9	897	794 ± 7
YHXT14	62	178.5	1.69	1.7	901	655 ± 16
YHXT07	100	189.5	1.83	0.1	596	616 ± 5
YHXT08	100	189.5	1.83	0.9	600	640 ± 8
YHXT09	97	170.5	1.83	2.0	602	536 ± 28
YHXT10	62	180.0	1.83	0.1	894	878 ± 21
YHXT11	62	180.0	1.83	0.8	896	677 ± 19
YHXT12	62	178.5	1.83	2.0	903	672 ± 4
YHS01	100	184.5	1.87	2.0	600	532 ± 18
YHS03	100	174.5	1.87	2.0	599	597 ± 25

The HFIR irradiation capsule design accommodates 16  $\text{YH}_x$  disk specimens, 6-mm diameter and 0.5 mm thickness. The specimens are placed between SiC components including SiC thermometry (TM), retainer specimens, and retainer springs. All internal components are loaded into a molybdenum holder, that is then backfilled with ultra-high-purity helium and welded. The holder is loaded into an aluminum housing, that is backfilled with a helium/argon mixed gas and welded. The housing is directly cooled by HFIR coolant on its outside during irradiation. The average

specimen irradiation temperature is designed by the HFIR irradiation location, the size of the gas gap between the outer wall of the holder and the inner wall of the housing, and the helium/argon mixture. Additional details on the capsule design can be found in [6, 12]. Figure 2-1 shows the irradiation capsule design and Figure 2-2 shows the layout of the components prior to capsule assembly.

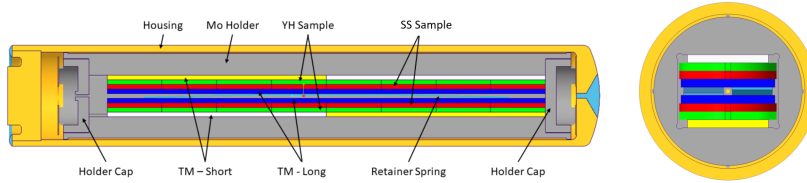


Figure 2-1 Irradiation capsule design [6, 7, 14]

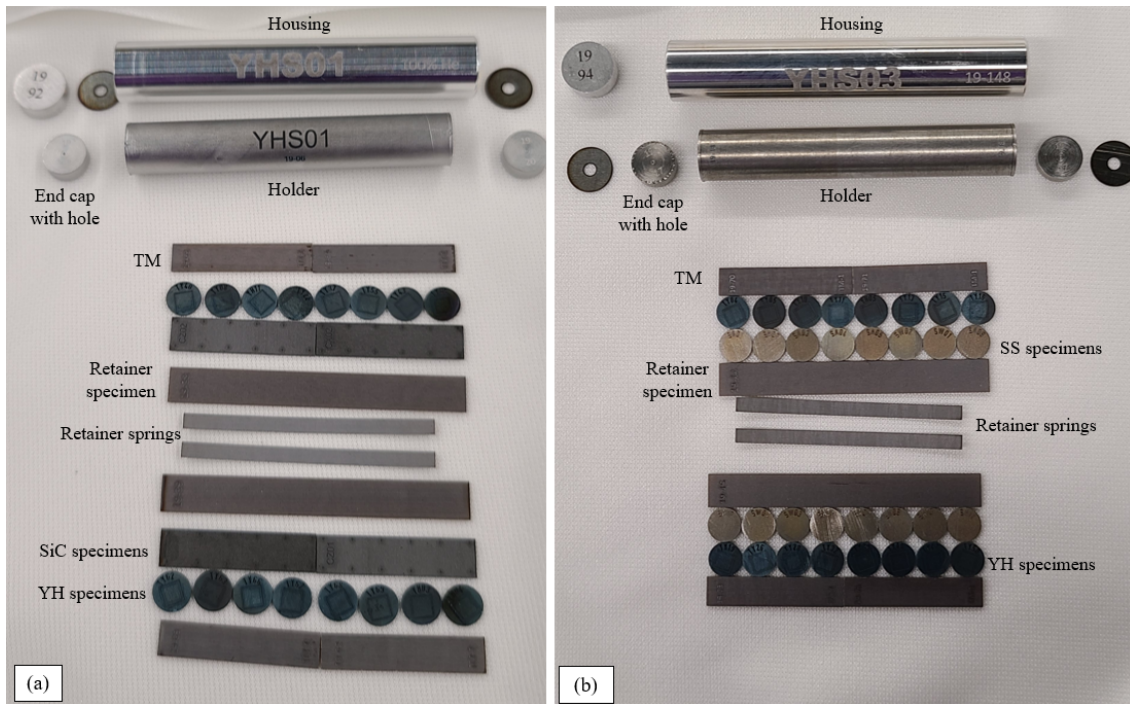


Figure 2-2 Capsule parts layout (a) YHS01 and (b) YHS03

The thermal design of the capsule was performed with ANSYS software to predict the components irradiation temperature using the components heat generation rates determined by neutronics calculation[6]. Figure 2-3 shows an example of the  $\text{YH}_x$  specimens temperature contours on a half-model of the capsule, for an average specimen temperature of  $600^\circ\text{C}$ . In this case, the temperature of the specimen varies from  $589$  to  $609^\circ\text{C}$ , depending on their location in the capsule. It should be noted the radial temperature difference per specimen is estimated as  $\pm 5^\circ\text{C}$ , where no significant Sore diffusion was expected within specimens. One consideration for temperature-gradient effects is related to the capsule cooling period after HFIR irradiation is terminated. This is currently unknown and further investigations are needed.

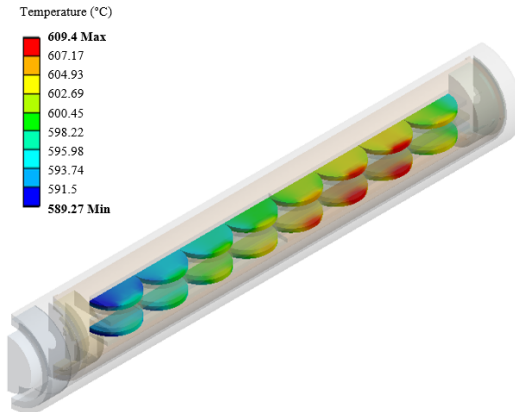


Figure 2-3 Representative temperature distribution in YH<sub>x</sub> specimens for a capsule design targeting an irradiation temperature of 600°C.

### 3. POST-IRRADIATION EXAMINATION PLAN

The PIE plan is mostly focused on the specimens from capsules YHS01 and YHS03, but included a subset of specimens from capsules YHXT07, YHXT08, and YHXT09. It includes a visual examination of the specimens, in addition to dimensional inspection, LFA for thermal diffusivity measurements, DSC for specific heat capacity measurements, microscopy analysis, and XRD analysis, on selected specimens. Table 3-1 presents a summary of the PIE plan. In addition, the PIE work includes the analysis of the SiC TMs to confirm the capsule irradiation temperature.

Table 3-1 Summary of the PIE

Capsule ID	Specimen ID	Post-irradiation examination					
		Visual	Dimensional	LFA	DSC	Microscopy	XRD
YHXT07	M004	X				X	
YHXT07	M013	X			X		
YHXT08	M007	X				X	
YHXT08	M011	X			X		
YHXT08	M081	X			X		
YHXT09	M100	X				X	
YHXT09	M088	X			X		
YHXT09	M052	X			X		
YHS01	TY08	X	X			X	
YHS01	TY22	X	X		X		
YHS01	TY37	X	X		X		
YHS01	TY40	X	X		X		
YHS01	TY43	X	X		X		
YHS01	TY55	X	X		X		
YHS01	TY62	X	X				X

YHS01	TY63	X	X	X			X
YHS01	TY65	X	X				X
YHS01	TY66	X	X	X			X
YHS01	TY67	X	X	X			X
YHS01	TY68	X	X		X		
YHS01	TY69	X	X		X		
YHS01	YH03	X	X		X		
YHS01	YH04	X	X		X		
YHS01	YH11	X	X		X		
YHS03	TY10	X	X		X		X
YHS03	TY11	X	X		X		X
YHS03	TY13	X	X		X		
YHS03	TY15	X	X		X		
YHS03	TY16	X	X	X	X		X
YHS03	TY19	X	X		X		
YHS03	TY04	X	X		X		
YHS03	TY05	X	X	X		X	
YHS03	TY26	X	X		X		
YHS03	TY28	X	X		X		
YHS03	TY32	X	X		X		
YHS03	TY39	X	X		X		
YHS03	TY46	X	X		X		
YHS03	TY47	X	X		X		
YHS03	TY50	X	X	X			X
YHS03	YH05	X	X		X		X

#### 4. SPECIMEN INSPECTION METHODS PRIOR TO IRRADIATIONS

Each specimen from capsules YHS01 and YHS03 was engraved with square marking at the center and on one side of the disk. Six dimensional measurements were recorded for each marking with a Keyence VHX digital microscope, including each side and each diagonal of the engraved square. Figure 4-1 shows a Keyence image of one specimen with recorded dimensional measurements. It is to note that the magnification used to allow accurate dimensional measurements of the markings did not allow for an image of the full disk specimen. Each dimension was labeled from 1 to 6, with the first measurement corresponding to the side of the engraved square right below the specimen engraved ID. The same measurements were recorded post-irradiation to assess dimensional changes of the specimens.



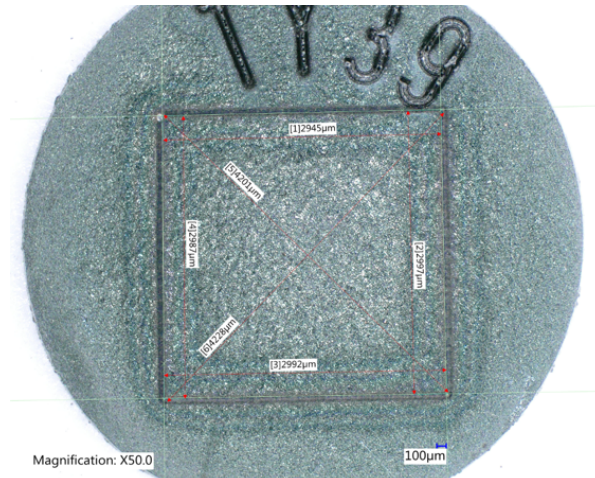


Figure 4-1 Keyence images of specimen TY39 with recorded measurements of the engraved markings pre-irradiation.

## 5. POST-IRRADIATION EXAMINATION

### 5.1 SiC passive thermometry analysis

The SiC TMs were analyzed via dilatometry in LAMDA following the standard ORNL procedure [15]. The average TM irradiation temperature (also referred to as experimental temperature) is derived from the dilatometry measurements [16, 17]. The average specimen experimental temperature is then derived from the average TM experimental temperature, applying the predicted difference of average temperature between TM and specimen from the numerical calculation.

### 5.2 Thermal property measurements

Thermal properties of specimens were determined via laser-flash analysis (LFA) and differential scanning calorimetry (DSC), see Figure 5-1, to determine thermal diffusivity and heat capacity, respectively. LFA measurements were performed using a Netzsch LFA 467 equipment by following ASTM E1461 [18] and ORNL standard operating procedure [19]. Data were collected within 50°C intervals from 25 to 800°C for heating. Data collection was limited to 600°C, 300°C, and 100°C during cooling. Heating curves were used to determine the thermal diffusivity. The heating and cooling rate for the LFA was 20°C/min with an argon gas flow of 40mL/min.

DSC was performed using a Netzsch DSC 404F1 equipment following [20] and ORNL standard operating procedure [21]. Specimens were subject of 1, 2, or 3 heating-cooling cycles to determine the change in the heat capacity as related to H/Y ratio changes. A representative cycle included (i) heating up to 800°C (ii) soaked at 800°C for 1 minute, (ii) cooling down to 30°C, and (iv) soak at 30°C for 30 minutes before the next cycle start. For the final heating cycle of 3-cycle treatment, the test was programmed to 5°C to captures as much data as possible. The heating and cooling rates were 20°C/min with an argon gas flow of 70mL/min.

Importantly, all measurements were conducted under inert conditions without control of H partial pressure, and the experiments did not adhere to pressure–concentration–temperature equilibrium curves. As a result, the derived thermal properties should be interpreted as quasi-intrinsic rather than absolute. Nevertheless, the data are suitable for engineering applications, particularly reactor modeling, given the high hydrogen retention stability observed under the initial heating conditions. In addition to property determination, further thermal cycling was applied to selected specimens to probe transition phenomena, which could inform the development of an approximate metric for hydrogen retention and redistribution. While thermal diffusivity measurements were performed on a limited subset of samples, DSC analysis was applied to a broader set to increase statistical robustness in heat capacity-based transition mapping.

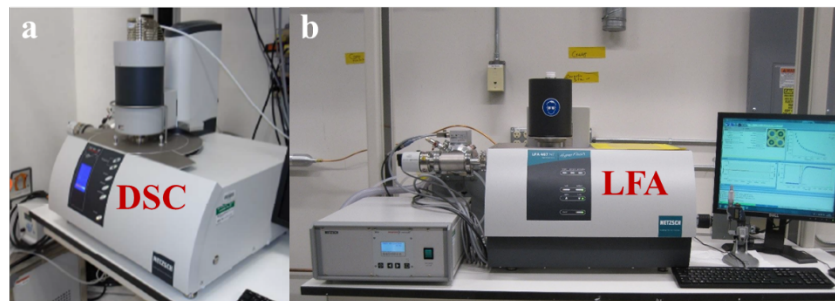


Figure 5-1 Pictures of (a) DSC and (b) LFA equipment located at LAMDA

Transition temperatures were determined from the specific heat vs temperature data. Because there was a hysteresis effect between heating and cooling cycles. Both are treated separately. The temperature determination used a local minimum and maximum determination algorithm by selecting temperature range of interest as shown in Figure 5-2.

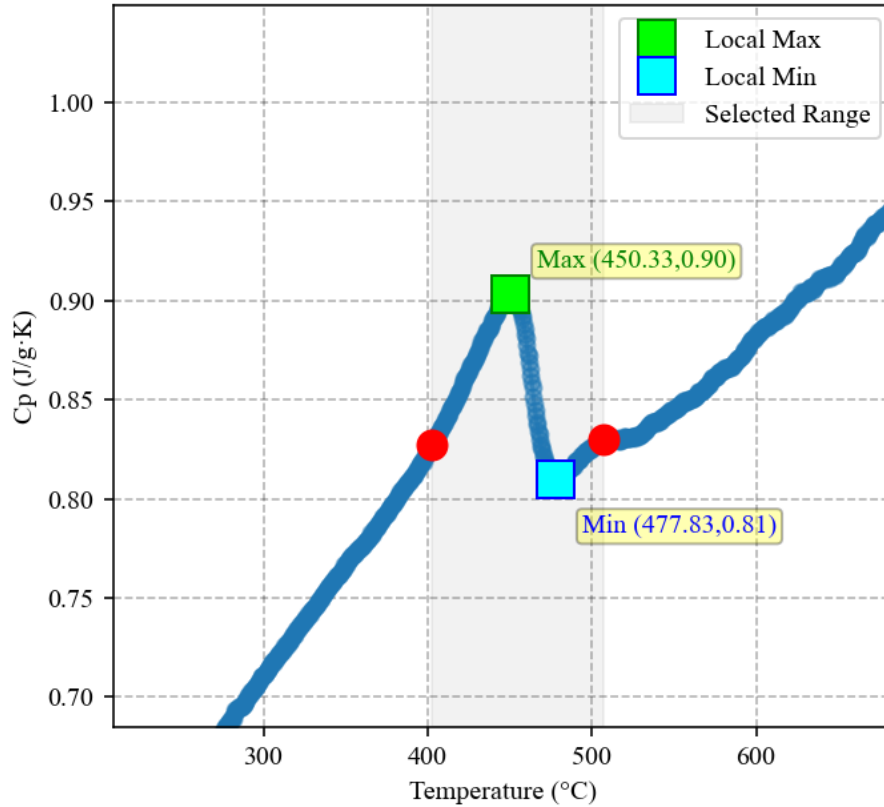


Figure 5-2 Depiction of transition temperature determination through finding local maximum and minimums.

### 5.3 TEM characterizations

Microstructure characterization of neutron-irradiated YHx samples was performed at the Low Activation Materials Development and Analysis (LAMDA) facility at ORNL. Cross-sectional TEM specimens were prepared using an FEI Versa 3D Dual Beam focused ion beam (FIB) scanning electron microscope (SEM), as illustrated in Figure 5-3. To protect the sample surface during milling, a  $\sim 2\ \mu\text{m}$  platinum (Pt) layer was deposited via a gas injection system, wherein a precursor gas was decomposed by the ion beam. Initial trenching was conducted using 30–50 kV gallium (Ga) ion beams, followed by thinning and lift-out steps at 15 kV and 7 kV, respectively. Final polishing of the lamellae was performed using lower-energy Ga ions at 5 kV and 2 kV.



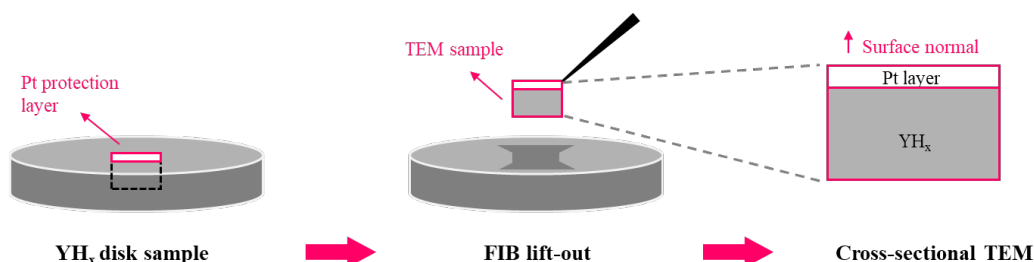


Figure 5-3 TEM specimen preparation procedure, specimens were not ground or polished at the outer surface to characterize the near surface microstructure from the hydrogen retention perspective.

The microstructure of the specimens was characterized using a JEOL JEM-2100F transmission electron microscope (TEM) operated at 200 kV. Scanning transmission electron microscopy–energy dispersive X-ray spectroscopy (STEM-EDS) was performed on an FEI Talos F200X TEM, also operated at 200 kV, with data processed using FEI Velox software. Spectrum images were acquired at a resolution of  $1024 \times 1024$  pixels with a dwell time of 50  $\mu$ s per pixel.

For dislocation and defect loop imaging, all samples were aligned to the [011] zone axis for on-zone bright-field STEM (STEM-BF) imaging. Cavities were analyzed using the Fresnel contrast technique under both under-focus and over-focus conditions. Loops and cavities were assumed to be circular in two-dimensional STEM projections, and their average diameters were manually measured using ImageJ software. For each sample and defect type, more than 200 defects were measured to ensure statistical significance.

Dislocation density was determined using the line-intercept method applied to STEM-BF images. Sample thickness was estimated using the electron energy loss spectroscopy (EELS) log-ratio method.

## 5.4 High-energy through-thickness XRD measurements

High resolution scanning x-ray diffraction measurements were performed in transmission mode at the 28-ID-1 (PDF beamline) at the NSLS-II facility at Brookhaven National Laboratory (BNL). The transmitted X-rays were collected with a two-dimensional silicon X-ray detector (Perkin - ELMER, pixel size = 200  $\mu$ m). A schematic representation of the XRD experimental setup is shown in Figure 5-4. The energy of the incident X-rays was 74.5 keV. The X-ray beam on the sample was focused to get a spot size of 300  $\mu$ m  $\times$  300  $\mu$ m. All diffraction data were acquired at room temperature. To improve statistics, multiple diffraction patterns were taken from different locations of the same sample.

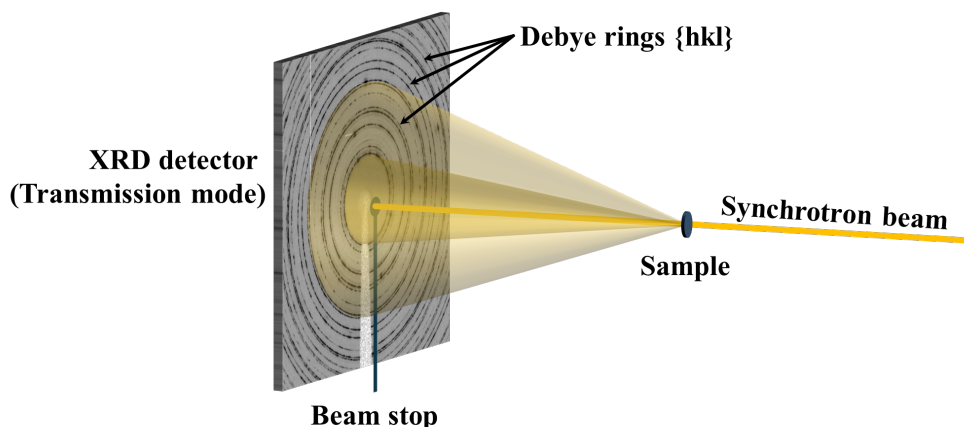


Figure 5-4 Schematic representation of synchrotron XRD experimental setup in transmission mode. The incident synchrotron beam passes through the sample, and the diffracted intensities are recorded by the XRD detector.

The captured images were processed and analyzed using XRDUA software. The first step in the XRD data analysis was the calibration of the XRD detector, and determination of the Bragg angles in relation to the positions of the diffraction spots appearing in the XRD images. For this purpose, quantitative XRD measurements have been made using a standard lanthanum hexaboride ( $\text{LaB}_6$ ) powder sample (reference material), for which the crystal structure is well known. This is an important step, which has been used to determine the sample-detector distance, the rotation and tilt angles of the detector and other global parameters related to the experimental setup.

An example of a two-dimensional diffraction pattern obtained from the  $\text{LaB}_6$  reference powder sample is shown in the inset of Figure 5-5. The 2D diffraction pattern of  $\text{LaB}_6$  powder reveals concentric Debye rings corresponding to various  $\{hkl\}$  reflection planes of the sample, captured out to  $14^\circ$  ( $2\theta$  value). This diffraction range, measured in units of  $2\theta$ , represents the scattering angle between the incident beam and the diffracted X-rays. The detection range depends on both the sample-detector distance as well as the width of the detector.

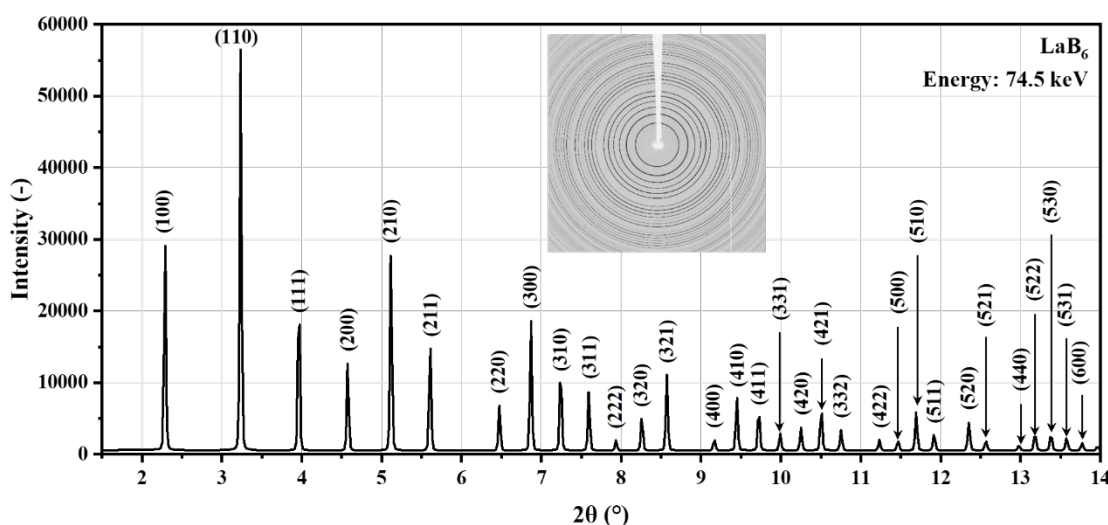


Figure 5-5 1D diffraction spectrum of reference  $\text{LaB}_6$  powder sample. The inset shows the corresponding 2D diffraction pattern measured at 74.5 keV energy.

Debye rings are the equivalent of Bragg's peaks in a 2D XRD image and each ring corresponds to a particular d-spacing or  $2\theta$  angle in a 1D diffraction spectrum. Since a direct correspondence exists between the radial coordinates and the peak positions in the XRD spectrum, integration over a given angular range has been performed in the radial direction to obtain the average peak intensities versus  $2\theta$  plots, as shown in Fig. 5-4 as an example.

The next step was the analysis of the XRD data measured from non-irradiated and irradiated  $\text{YH}_x$  specimens. The pixel intensities in each 2D-XRD image were integrated radially to yield corresponding 1D-XRD pattern. Selected diffraction  $\{hkl\}$  peaks were fitted using a symmetric Pseudo-Voigt function to determine the angular centroid positions ( $2\theta_{hkl}$ ) and full width at half-maximum (FWHM) in the 1D line profile analyses.

Yttrium dihydride ( $\text{YH}_2$ ) belongs to the fluorite crystal family, and its crystalline structure takes the  $\text{Fm}\bar{3}\text{m}$  (225) space group. In a perfectly stoichiometric and well-crystallized product, the Y-atoms form a face-centered cubic (FCC) lattice, and the H-atoms occupy the tetrahedral sites within that lattice. On the other hand, metallic yttrium typically crystallizes in a hexagonal close packed (hcp) structure with space group  $\text{P6}_3/\text{mmc}$ .

## 6. RESULTS

### 6.1 SiC passive thermometry

Figure 6-1 shows the predicted and experimental average specimen temperature for each capsule. These results, also shown in Table 21, show overall a good agreement between predicted and experimental temperatures. Capsules YHXT11, YHXT12, and YHXT14 show the largest difference between predicted and experimental temperatures.

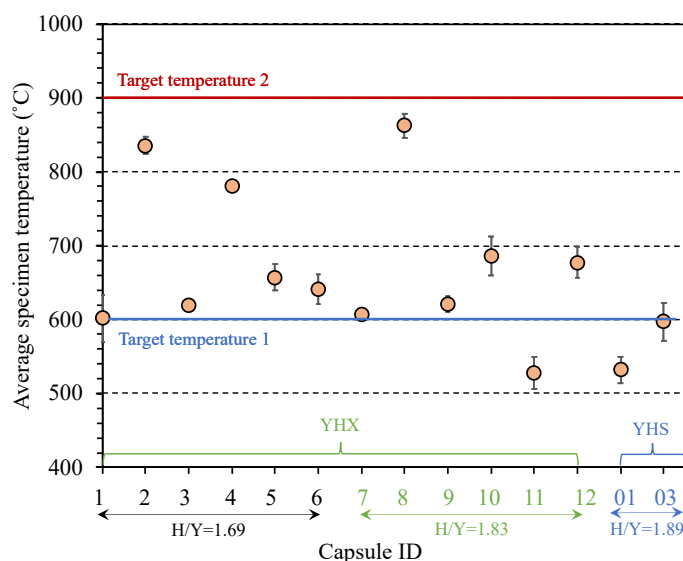



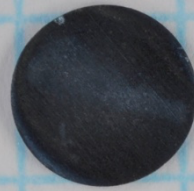

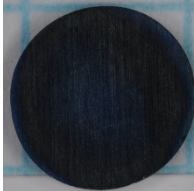

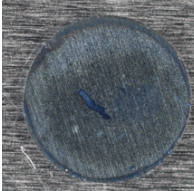




Figure 6-1 Predicted and experimental average specimen temperature for each  $\text{YH}_x$  capsule.

### 6.2 Visual Examination

Table 6-1 shows the optical pictures of specimens after HFIR irradiation. Specimens tested from YHX07-09 had initial H/Y ratio of 1.83 and the irradiation temperature of all specimens were

~600°C and the dose levels ranged from 0.1, 0.9, and 2 dpa. Specimens from capsule YHX07 had darker blue color on both sides, indicating higher H/Y ratio while specimens from other two capsules either one or both sides were lighter blue suggesting lower H/Y ratio. This implied that these specimens lost some H during irradiation if the initial H/Y ratio was ~1.83. While this discoloration was first glance related to irradiation dose, specimen pictures from YHS01 and 03 had both darker and lighter blue color within the sample capsule, which suggested that H redistribution between specimens.

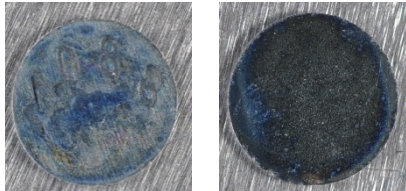
Table 6-1 Specimen list and pictures. For scale: diameter of a specimen is about 6 mm

Capsule Specimen	Specimen pictures	
	Front	Back
YHXT07 M004		
YHXT07 M013		
YHXT08 M007		
YHXT08 M011		
YHXT08 M081		

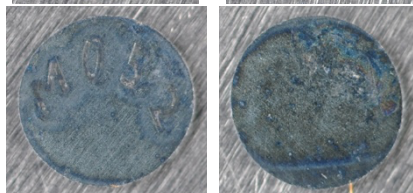
YHXT09 M100



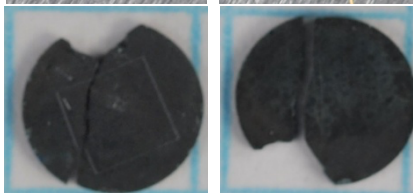
YHXT09 M088



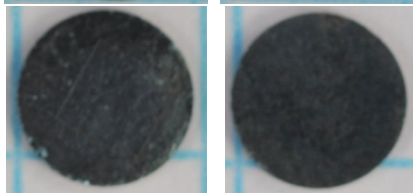
YHXT09 M052



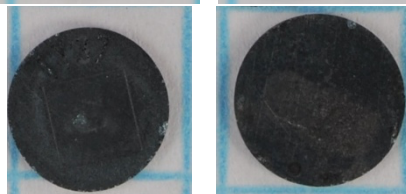
YHS01 TY08



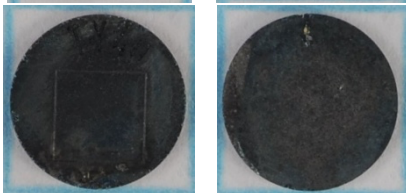
YHS01 TY22



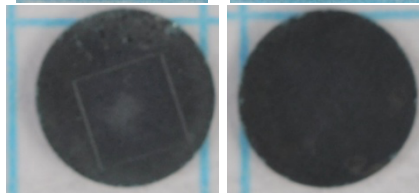
YHS01 TY37



YHS01 TY40



YHS01 TY43



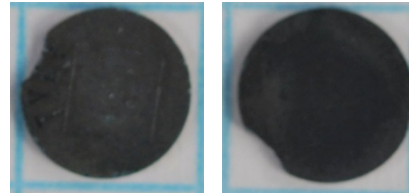
YHS01 TY55



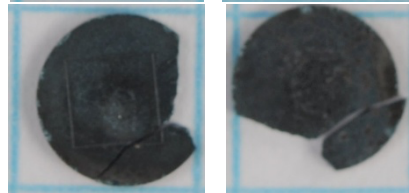
YHS01 TY62



YHS01 TY63



YHS01 TY65



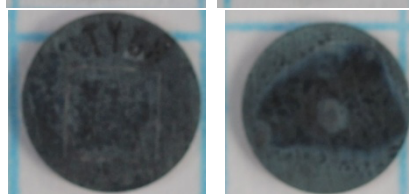
YHS01 TY66



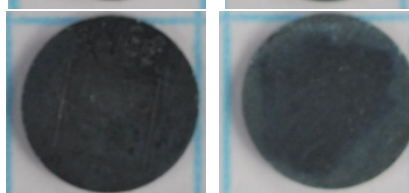
YHS01 TY67



YHS01 TY68

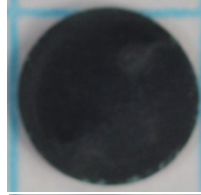
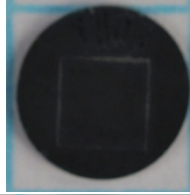


YHS01 TY69

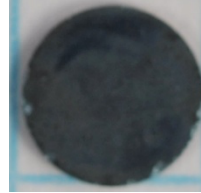




YHS01 YH03



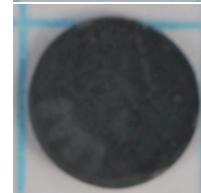
YHS01 YH04



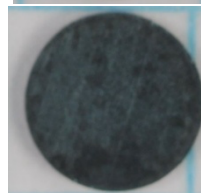
YHS01 YH11



YHS03 TY10



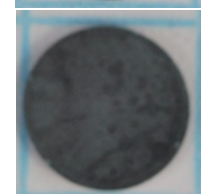
YHS03 TY11



YHS03 TY13



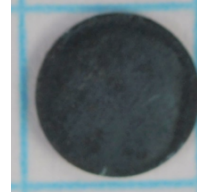
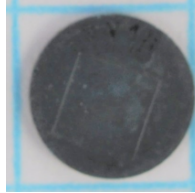
YHS03 TY15



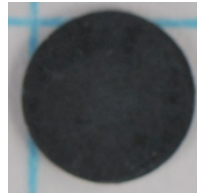
YHS03 TY16



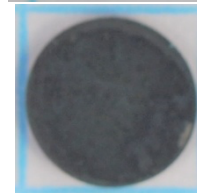
YHS03 TY19



YHS03 TY04



YHS03 TY05



YHS03 TY26



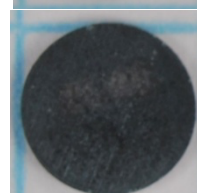
YHS03 TY28



YHS03 TY32



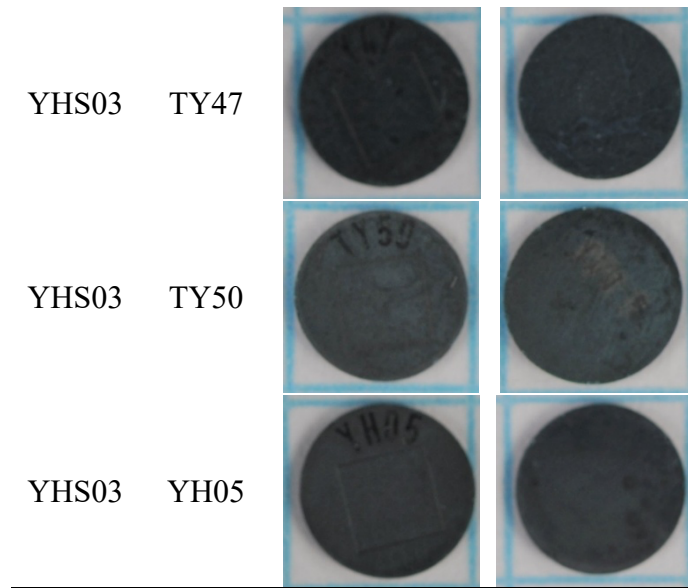
YHS03 TY39



YHS03 TY46







### 6.3 Dimensional change

Figure 6-2 summarizes the specimen dimensional change results. The 6 engraved dimensions were recorded for each of the 16 YH<sub>1.87</sub> specimens of each capsule. Each dimension is shown on Figure 6-2 with the dimension number in the x-axis, and the corresponding dimension location in yellow on the disk images at the top. The average dimensional change in the figure corresponds to the average of the 6 dimensions. Each data point represents the dimensional change for one specimen. The average dimensional change per capsule is shown with the histograms, with the error bars representing the standard deviation for the specimens from the same capsule. Overall, the specimens exhibited good dimensional stability under irradiation with a slight shrinkage reported at each measurement location.

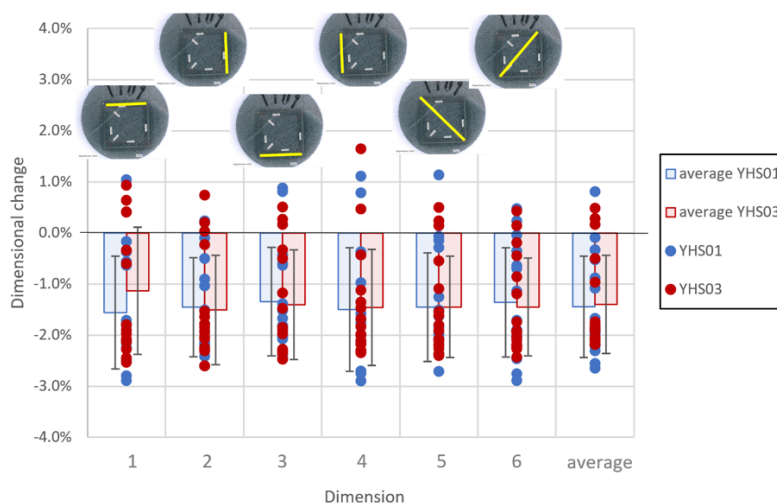
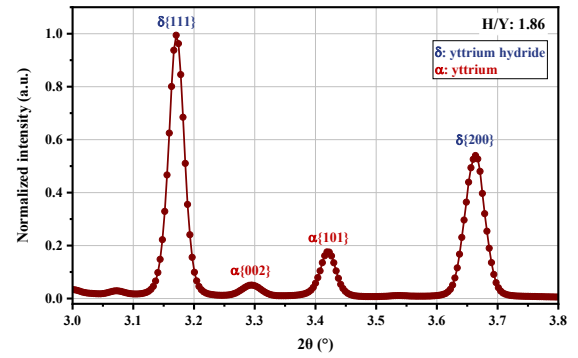
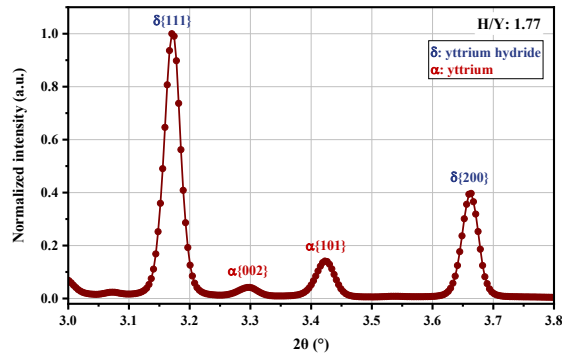
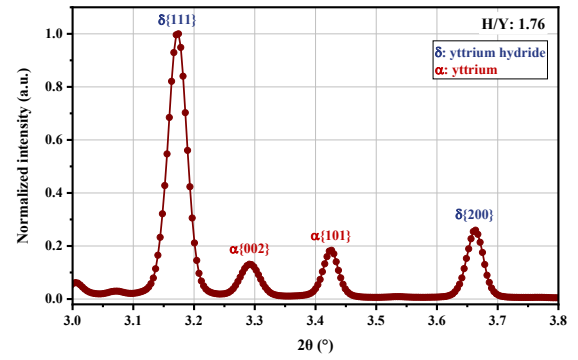
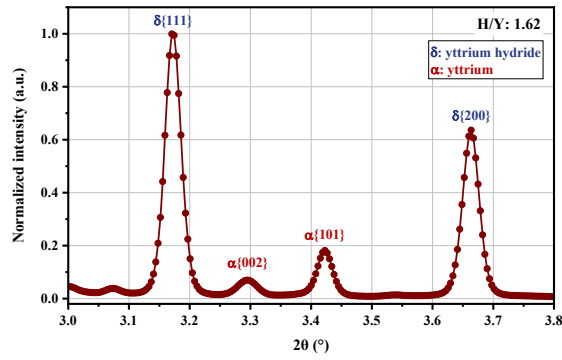
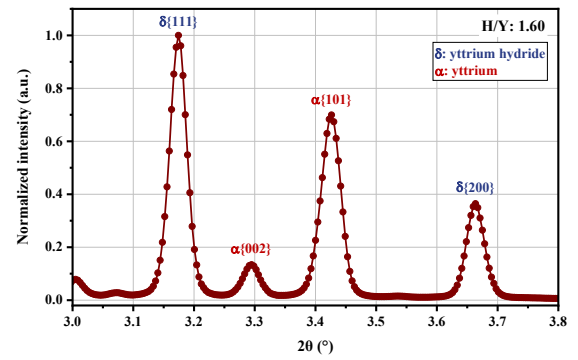
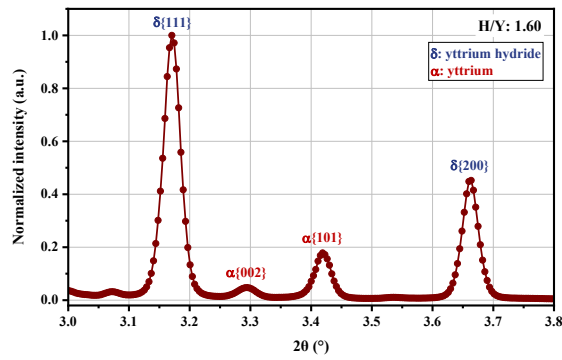
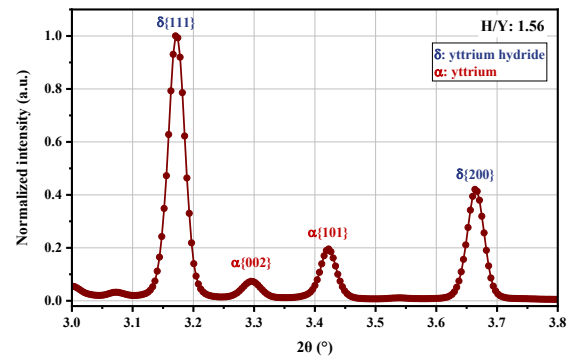
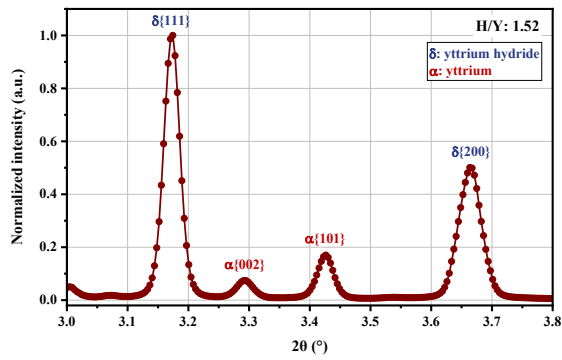


Figure 6-2 Dimensional change measured at 6 locations between engraved lines (depicted with a yellow line). Each data point is the dimensional change for an individual specimen. The average dimensional change relative to the pre-irradiation measurement at each location is plotted as a histogram with standard deviation of the measurement shown on the error bar.

## 6.4 Synchrotron XRD analysis

Previous PIE work performed at INL and ORNL on yttrium hydrides have indicated the redistribution of hydrogen within the sample matrix as a consequence of irradiation[10]. The extent of hydrogen gains or losses is not uniform for all the samples, and is a function of the irradiation history of the sample (temperature, displacement damage, *etc.*). In this regard, it is important to have a robust hydrogen retention metric and investigate the phase fraction variations in irradiated  $\text{YH}_x$  specimens. For this purpose, high-brilliance synchrotron light-based XRD was performed on both non-irradiated and irradiated  $\text{YH}_x$  specimens. The XRD measurements were done in the transmission mode, and hence, the obtained diffractograms contained volume information from the bulk specimen. Also, the high photon flux of synchrotron enabled to study the subtle changes in the yttrium to hydrogen ratio.

Room temperature line profiles of non-irradiated  $\text{YH}_x$  specimens are shown in Figure 6-3. Each of the individual XRD spectra is a summation of multiple patterns, representative of the entire bulk sample. The main hydride and yttrium phases are illustrated in blue and red, respectively.  $\text{YH}_2$  has a face-centered cubic (fcc) structure, whereas Y has a hexagonal closed packed (hcp) crystal structure. No  $\epsilon$  hydrides were detected.



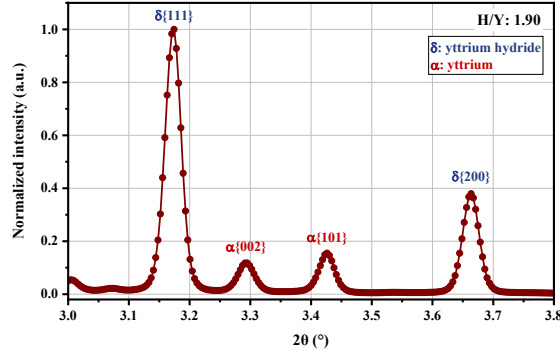


Figure 6-3 Experimental XRD patterns of non-irradiated  $\text{YH}_x$  specimens having different stoichiometries ranging from 1.52 to 1.90.

The relative intensities of  $\alpha$ -Y and  $\delta$ - $\text{YH}_2$  peaks change as a function of stoichiometry. With increase in the hydrogen volume fraction, the  $\delta$ - $\text{YH}_2$  peak intensities increase along with a subsequent reduction of  $\alpha$ -Y intensities. The dependence of peak intensity ratios of metallic yttrium and hydride phases on the stoichiometry is tabulated in Table 6-2.

Table 6-2: XRD peak intensity ratios of non-irradiated  $\text{YH}_x$  specimens having different stoichiometries

H/Y	$\alpha\{101\} / \delta\{111\}$
1.52	0.175
1.56	0.194
1.60	0.174
1.60	0.763
1.62	0.180
1.76	0.153
1.77	0.160
1.86	0.187
1.90	0.154

Figure 6-4 presents the ratio of  $\{101\}$  peak intensity of  $\alpha$ -Y and  $\{111\}$  peak intensity of  $\delta$ - $\text{YH}_2$  phases. Note that the red dotted line is drawn to guide the eye. Barring a few outliers, the  $\alpha\{101\}/\delta\{111\}$  intensity ratios follow a decreasing trend with increasing H/Y stoichiometric ratios.

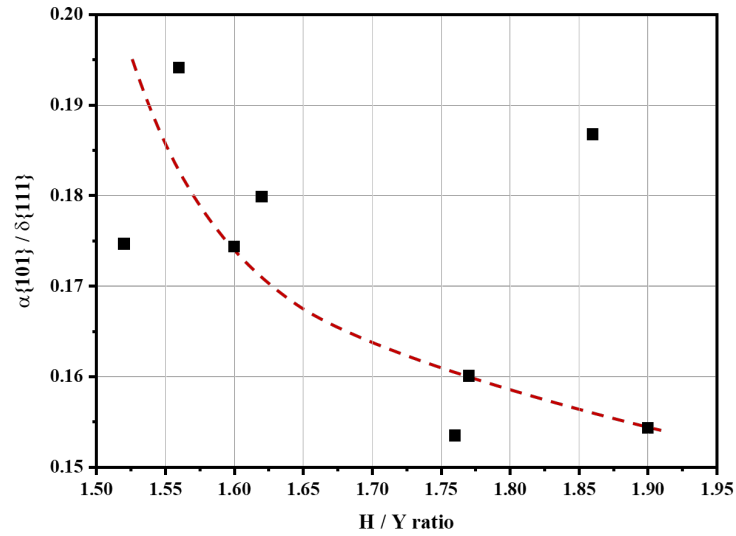


Figure 6-4 Changes in the peak intensities of  $\alpha$ -Y and  $\delta$ -YH<sub>2</sub> due to stoichiometry of YH<sub>x</sub> specimens. The red dotted line is to guide the eye.

Neutron irradiation is known to impact the hydrogen retention behavior in YH<sub>x</sub>. To investigate the irradiation-induced effects, a set of HFIR-irradiated YH<sub>x</sub> specimens were analyzed using identical synchrotron XRD experimental setup. Room temperature line profiles of the irradiated YH<sub>x</sub> specimens in capsules YHS01 and YHS03 are shown in Figure 6-5 and Figure 6-6, respectively.

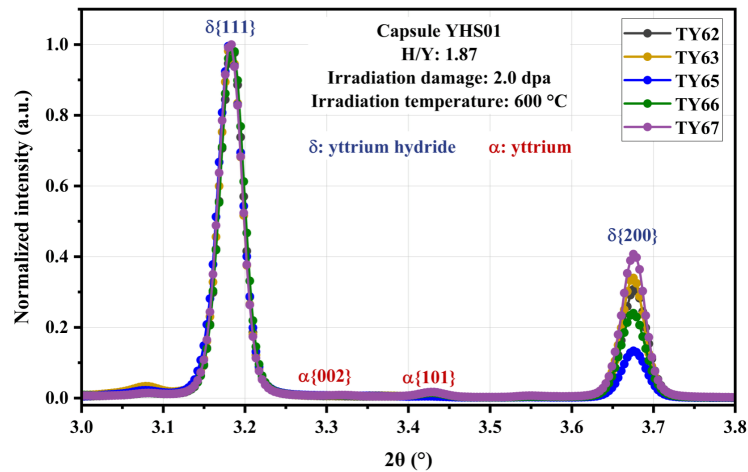


Figure 6-5 Experimental XRD patterns of irradiated YH<sub>x</sub> specimens in capsule YHS01.

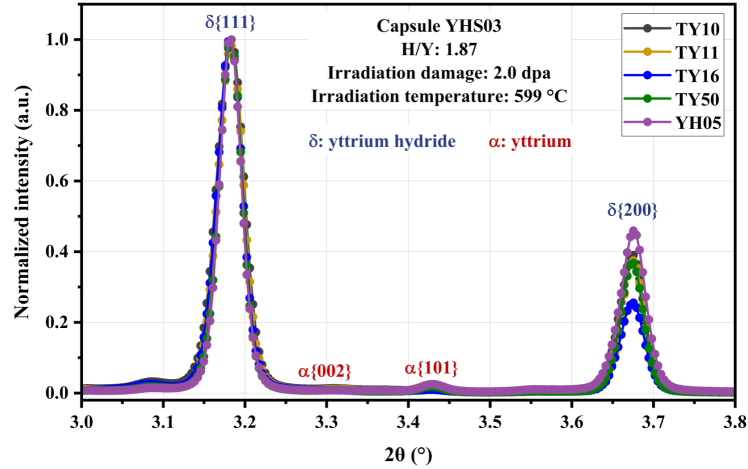


Figure 6-6 Experimental XRD patterns of irradiated  $\text{YH}_x$  specimens in capsule YHS03.

The XRD results indicate that the high-dose (2.0 dpa) neutron-irradiated  $\text{YH}_x$  specimens showed significant H retention at 600 °C. As can be seen in the line profiles of non-irradiated specimens (shown in Figure 6-3), the metallic yttrium peaks are much less intense relative to the hydride peaks. For the irradiated specimens (Figure 6-5 and Figure 6-6), the  $\alpha$ -Y metallic peaks are not distinctly visible, indicating that the specimens preserved their H content. The peak intensity ratios for the irradiated specimens are noted in Table 6-3.

Table 6-3 XRD peak intensity ratios of irradiated  $\text{YH}_x$  specimens

Capsule	Specimen ID	$\frac{\alpha\{101\}}{\delta\{111\}}$	Capsule	Specimen ID	$\frac{\alpha\{101\}}{\delta\{111\}}$
YHS01	TY62	0.017	YHS03	TY10	0.017
	TY63	0.015		TY11	0.026
	TY65	0.008		TY16	0.013
	TY66	0.018		TY50	0.021
	TY67	0.021		YH05	0.030

Though the relative intensities of the major diffraction peaks change under different irradiation conditions, their angular positions ( $2\theta$  values) remains a constant. This implies that despite hydrogen loss, the individual unit cells maintain structural stability independent of the irradiation history of the specimen. From the  $\delta$ -peaks, the lattice parameter of substoichiometric yttrium dihydride ( $\text{YH}_2$ ) is calculated as 5.210 Å.

## 6.5 Microscopy results

Characterization of the near-surface peripheral microstructure is critical for understanding hydrogen (H) loss behavior during operation, as H escape occurs through the specimen boundary. Therefore, detailed microstructural analysis supports component design by informing both H loss model development and alloy or structure optimization.

Figure 6-7 presents the microstructure near the specimen periphery using low-magnification STEM-BF images. Two main regions are distinguishable in the micrographs: (i) a

dark gray region corresponding to hydrides, and (ii) a light gray region corresponding to an amorphous phase. The latter was confirmed as amorphous based on electron diffraction patterns that exhibited no discrete diffraction spots but rather diffuse scattering, characteristic of non-crystalline structures.

While the amorphous region may originate from fabrication processes, the current results reveal a neutron dose-dependent trend in its thickness. Specifically, the amorphous layer thickness decreased with increasing neutron dose (see Figure 6-8), suggesting a possible amorphous-to-crystalline (a-to-c) transformation under neutron irradiation. This behavior is consistent with phenomena reported in metallic glasses and ceramics under ion irradiation. Elemental analysis further revealed that the amorphous region primarily consists of Y and O, with Ga and Pt excluded as artifacts from sample preparation. These findings suggest a potential a-to-c transformation, warranting further data collection for confirmation

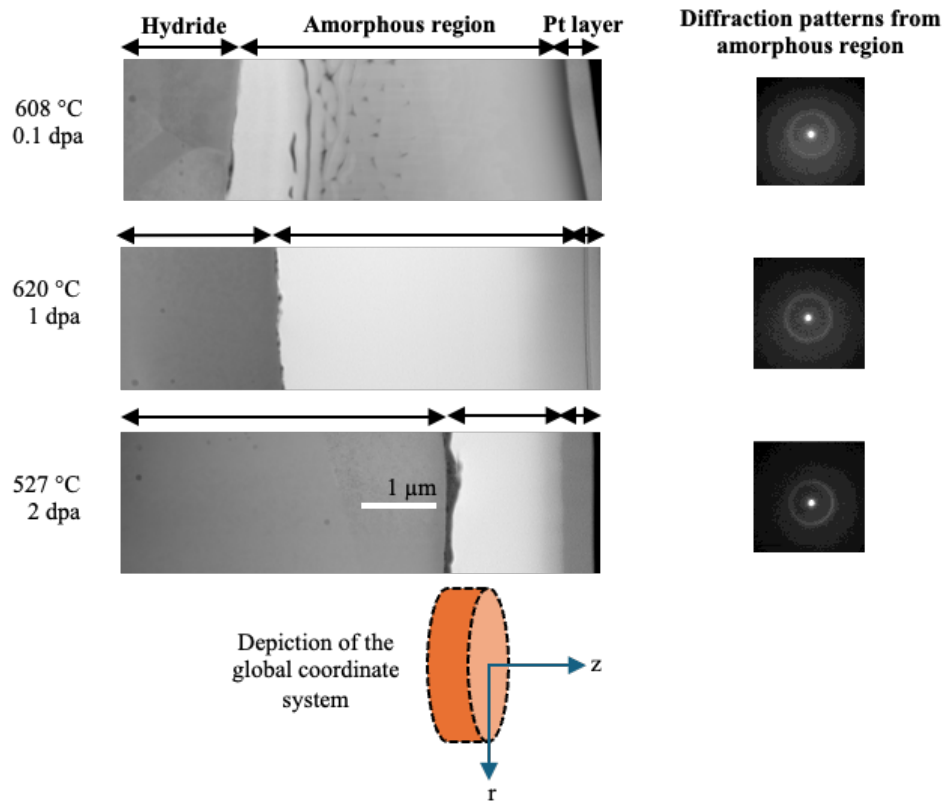


Figure 6-7 Microstructure near specimen periphery and diffraction patterns from the amorphous region

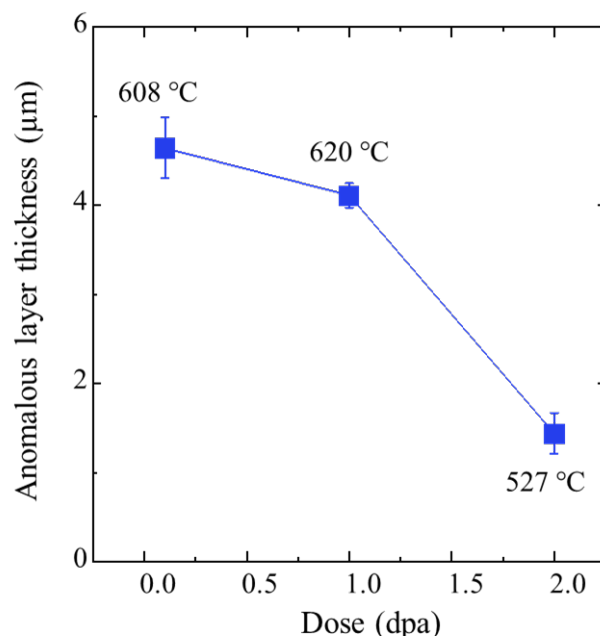


Figure 6-8 Thickness of the amorphous region with respect to neutron dose and irradiation temperature

Another key observation at the periphery was the presence of oxide islands or layers at the interface between the hydride and amorphous regions. Figure 6-9 shows STEM-ADF images and corresponding oxygen EDS maps, highlighting oxygen segregation and oxide layer formation at this interface. At low displacement damage (0.1 dpa), a semi-continuous O-rich layer and discrete oxide islands were observed. With increasing damage (1 dpa), a continuous oxide layer formed, accompanied by a higher oxygen concentration near the interface. This suggests the possibility of oxygen diffusion from the  $YH_x$  matrix to the interface. For the highest dose specimen (2 dpa), the oxide layer thickness increased to approximately 150 nm (Figure 6-9d), with localized thickening near tantalum (Ta) impurity particles<sup>1</sup>

<sup>1</sup> Ta, Ca, O, and other impurities were present in the initial yttrium stock materials due to their mining-to-fabrication route. The neutronic design must consider the elemental composition of initial yttrium stock material, and nuclear-grade yttrium must be defined.



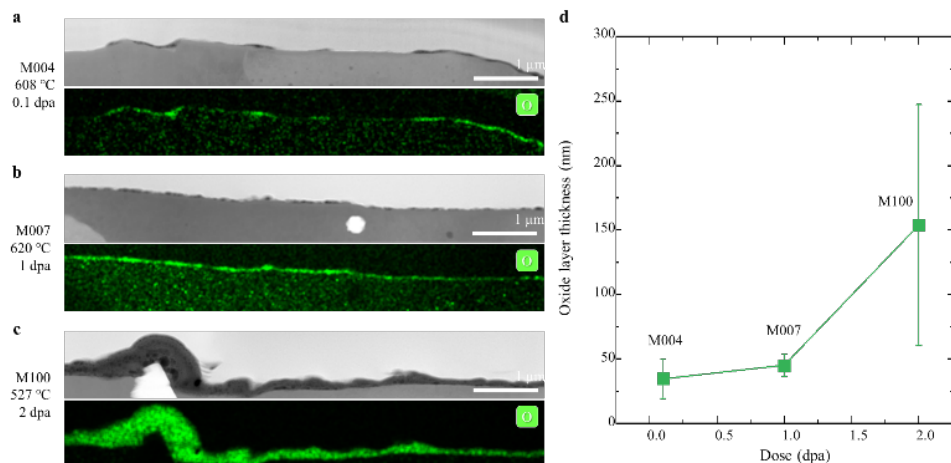


Figure 6-9 STEM-ADF images and EDS maps of O distribution at the interface of amorphous and hydride regions for specimens of (a) 0.1 dpa, (b) 1 dpa, and (c) 2 dpa; (d) oxide layer thickness vs neutron dose

A more detailed elemental map of the interface region (see Figure 6-10), showed the presence of Ca-rich (likely  $\text{CaF}_2$ ) and Ta precipitates near the interface. However, no segregation of Ca or other impurities, except for oxygen, was detected directly at the hydride–amorphous boundary. These precipitates are likely inherited from the initial Y stock material.

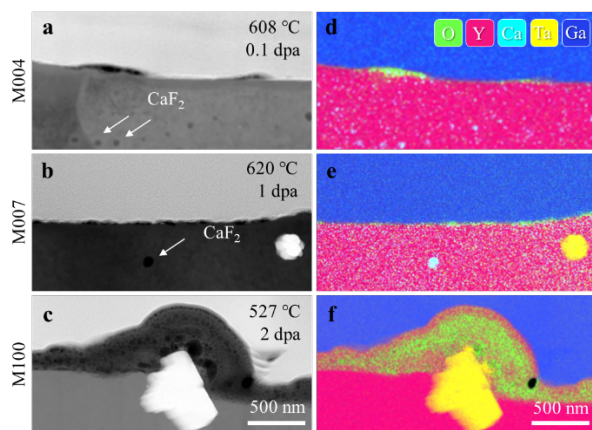


Figure 6-10 (a-c) STEM-ADF image and (d-f) EDS maps of near interface microstructure of specimens

S/TEM analysis of the hydride matrix (Figure 6-11) reveals distinct Ca and F elemental distributions in EDS maps, consistent with the presence of  $\text{CaF}_2$  precipitates. Quantitative evaluation (Figure 6-12) shows that both the density and average diameter of  $\text{CaF}_2$  precipitates decrease with increasing neutron dose. This trend, together with the microstructural features observed near the hydride–amorphous interface, suggests an evolution in local chemistry driven by  $\text{CaF}_2$  precipitate dissolution, radiation-induced diffusion, and elemental segregation. These findings point to active redistribution of impurity species under neutron irradiation.

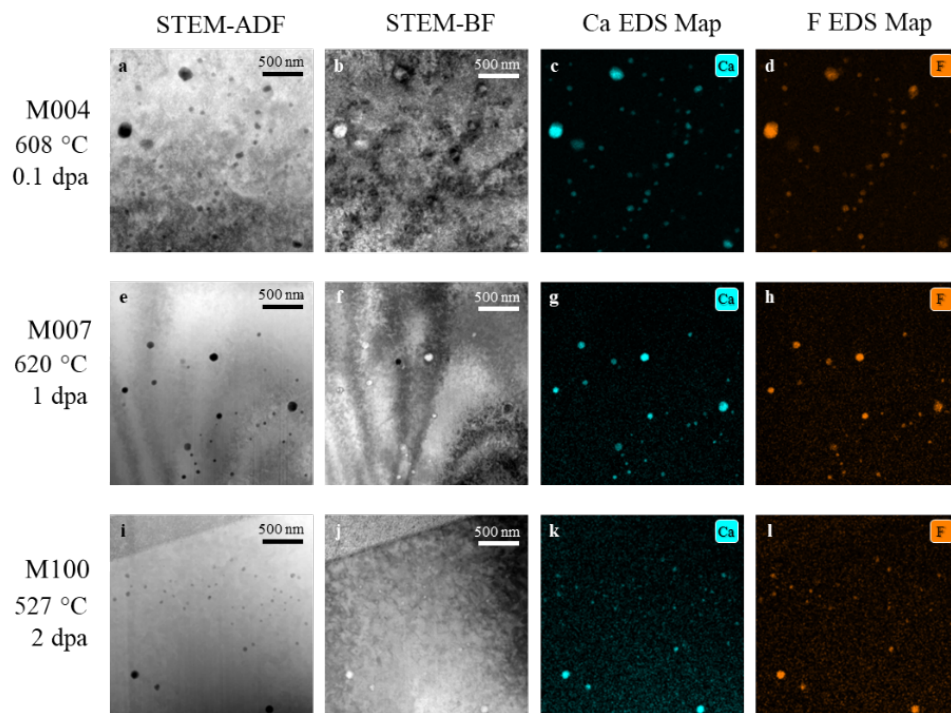


Figure 6-11 STEM images and EDS Ca and F elemental maps of irradiated yttrium hydride specimens

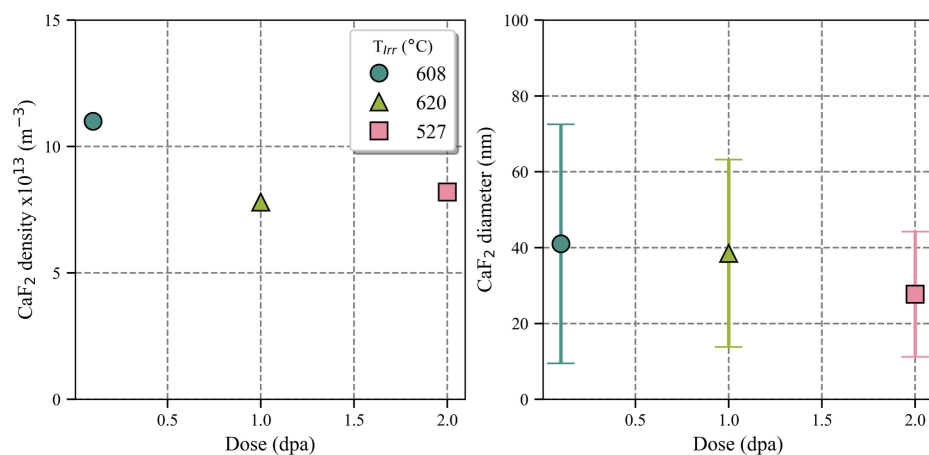


Figure 6-12 CaF<sub>2</sub> precipitate density and diameter as a function of neutron dose

Irradiation-induced dislocation loops exhibited varying spatial distributions depending on the neutron dose and irradiation temperature, as shown in Figure 6-13. For the 0.1 dpa specimen, loops were predominantly aligned along pre-existing dislocations or located near CaF<sub>2</sub> precipitates. In contrast, for the 1 dpa specimen, irradiated at a similar temperature, loops appeared randomly distributed, indicating a reduced influence of existing microstructural features on loop formation. At 2 dpa, irradiated at a lower temperature (527 °C), loops were again observed to align with pre-existing dislocations, suggesting a possible temperature-dependent alignment behavior.

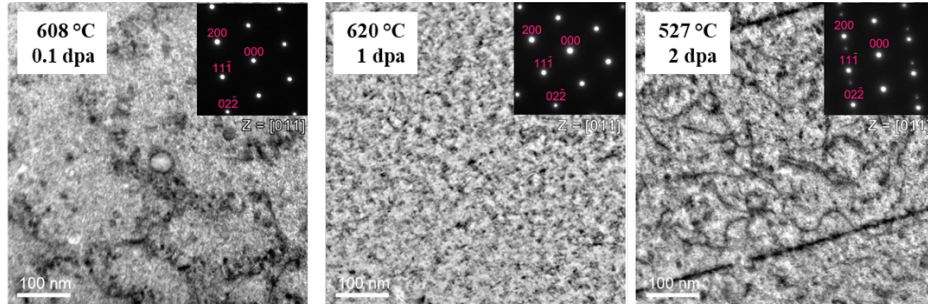


Figure 6-13 STEM-BF images showing dislocation loop microstructure in  $\text{YH}_x$  matrix for different irradiation conditions

Quantitative analysis (Figure 6-14) revealed that loop density increased significantly, from  $2.5 \times 10^{21} \text{ m}^{-3}$  at 0.1 dpa to  $11.1 \times 10^{21} \text{ m}^{-3}$  at 1 dpa, indicating a strong correlation between neutron displacement damage and loop nucleation. A further increase in loop density was also observed at 2 dpa, affirming the cumulative impact of displacement damage. In contrast, loop diameter remained relatively constant across all irradiation conditions, with values comparable to typical black-dot features, which are associated with small interstitial or vacancy clusters.

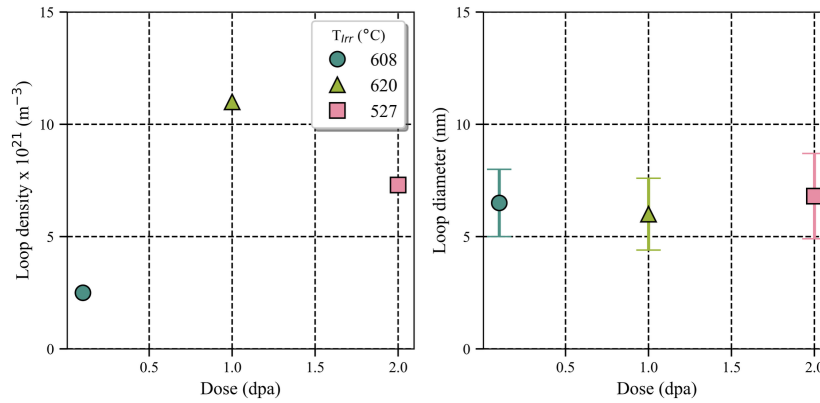


Figure 6-14 Dislocation loop density and diameter as a function of neutron dose

Furthermore, Figure 6-15 shows the cavity microstructure in  $\text{YH}_2$  matrix, consistent with observations from prior studies on the same specimens [12, 13]. Figure 6-16, the cavity number density was low at 0.1 dpa, but exhibited an approximately twofold increase with increasing neutron displacement damage. Notably, the average cavity diameter remained constant across all irradiation conditions, indicating no apparent dependence on either dose or irradiation temperature. A key finding from this dataset is that the observed increase in cavity number density was primarily driven by neutron displacement damage and appeared to be independent of temperature effects.

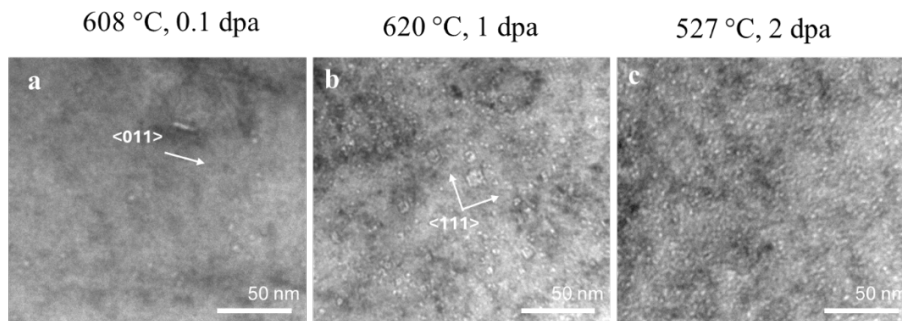


Figure 6-15 TEM under-focused images showing cavity microstructure in  $\text{YH}_x$  matrix for different irradiation conditions

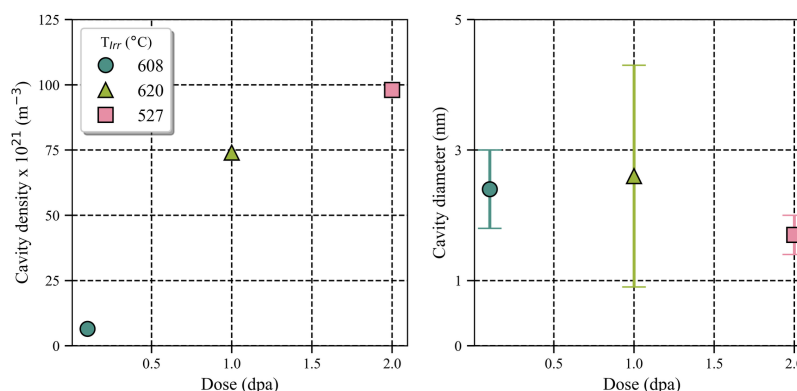


Figure 6-16 Cavity density and diameter as a function of neutron dose

To summarize, neutron irradiation induced a series of microstructural features in  $\text{YH}_x$ , with effects that span possibly amorphization, impurity behavior, interstitial and vacancy cluster formation. At the specimen periphery, it is likely that irradiation led to a progressive thinning of a pre-existing Y–O amorphous layer with increasing dose. Concurrently, O segregation at the hydride–amorphous interface caused the formation and thickening of an oxide layer, independent of irradiation temperature. Impurity phases such as  $\text{CaF}_2$  and Ta-rich precipitates were identified near interfaces, with  $\text{CaF}_2$  showing a decline in both density and size as dose increases, indicating dissolution and radiation-enhanced diffusion. Dislocation loops density increased with increasing neutron damage, while their size remained constant. A similar behavior was also observed for the irradiation induced cavities. These combined results suggested that neutron displacement damage is the dominant factor controlling defect density and size, while temperature was playing a secondary role with respect to current dataset. Further investigations were suggested to confirm the observations of the dataset.

## 6.6 Thermal property results

### 6.6.1 LFA results

Accurate thermal property data are essential for nuclear fuel performance modeling, particularly for evaluating temperature gradients in moderators as a function of local H concentration. In this context, the temperature-dependent behavior of sub-stoichiometric yttrium hydride ( $\text{YH}_x$ ) is of interest due to its correlation with the H/Y ratio, which may serve as an indirect indicator of hydrogen retention under irradiation and thermal cycling. To quantify

thermal transport properties, neutron-irradiated  $\text{YH}_x$  specimens were characterized using LFA for thermal diffusivity and DSC for specific heat capacity. Due to the probability of hydrogen desorption at elevated temperatures, only the first heating cycle was used to extract material properties, as subsequent cycles may reflect altered stoichiometry or microstructural evolution.

Figure 6-17 and Figure 6-18 show the thermal diffusivity data of specimens from capsules YSH01 and YHS03. Inset pictures correspond to the specific test specimen after disassembly before the experiment. The diffusivity of specimens in the same capsule showed similar behavior. Additionally, capsule wise comparison also indicated no significant variation in the thermal diffusivity. This observation was expected since specimens in capsules YSH01 and 03 had nominally the same H/Y ratio and were subject to the same irradiation conditions. The only difference was one set of specimens were in contact with SiC discs and the other set was in contact with stainless steel.

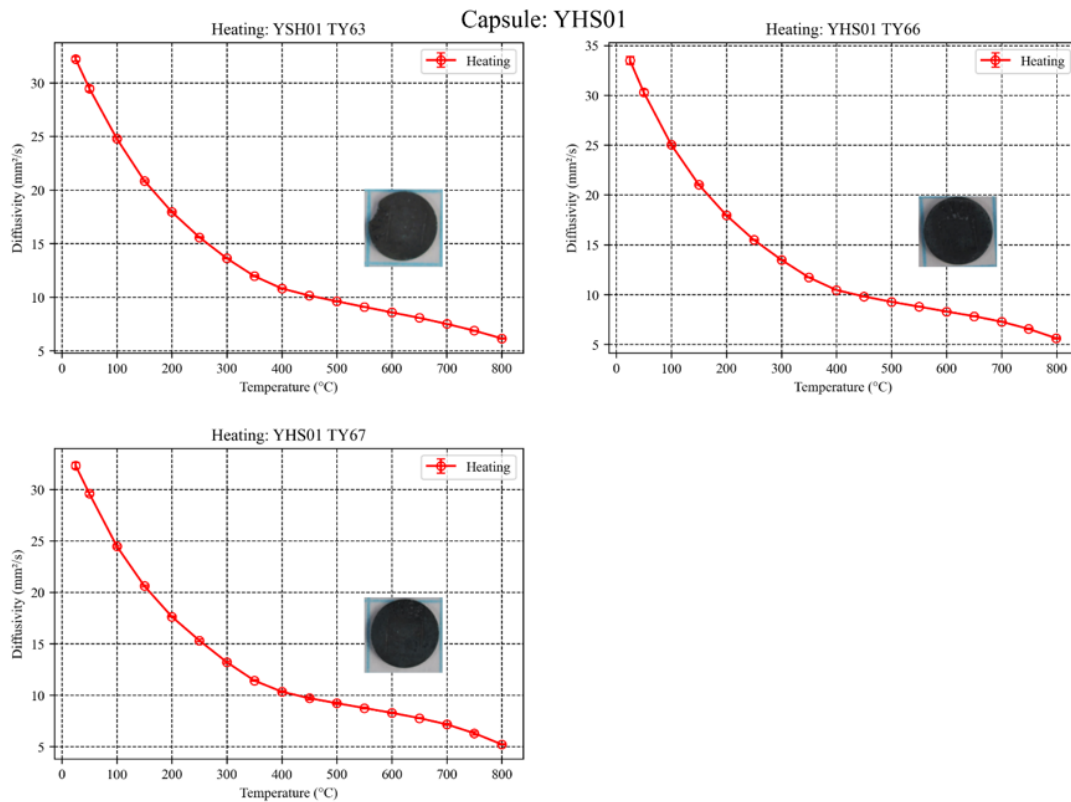


Figure 6-17 Thermal diffusivity of specimens (as-fabricated H/Y ratio was 1.87) irradiated at  $532^{\circ}\text{C}$  up to 2 dpa. (TY63, TY66, and TY67 from capsule YHS01)



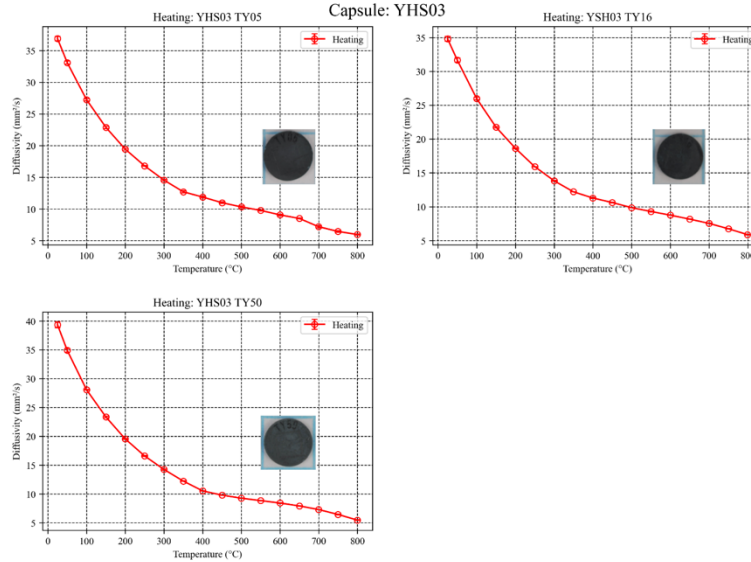


Figure 6-18 Thermal diffusivity of specimens (as-fabricated H/Y ratio was 1.87) irradiated at 597°C up to 2 dpa. (TY05, TY16, and TY50 from capsule YHS03)

All specimens showed a  $1/(A+BT)$  behavior like insulators and semiconductors, indicating phonon-dominated thermal transport; where A corresponds to defect, impurity and boundary scattering and B is the phonon-phonon (Umklapp) scattering term. To determine A and B, specimens per capsule were averaged and fitted to a curve  $1/(A+BT)$ .

Figure 6-19a and b show the fit results and compares a couple of literature values from similar as fabricated specimens for similar temperature ranges [9, 22]. Thermal diffusivity of irradiated specimens was lower than that for as fabricated. It was mainly considered due to H loss to irradiation induced defects or capsule environment. It is assumed that the initial H contents were accurately determined prior to HFIR irradiation.

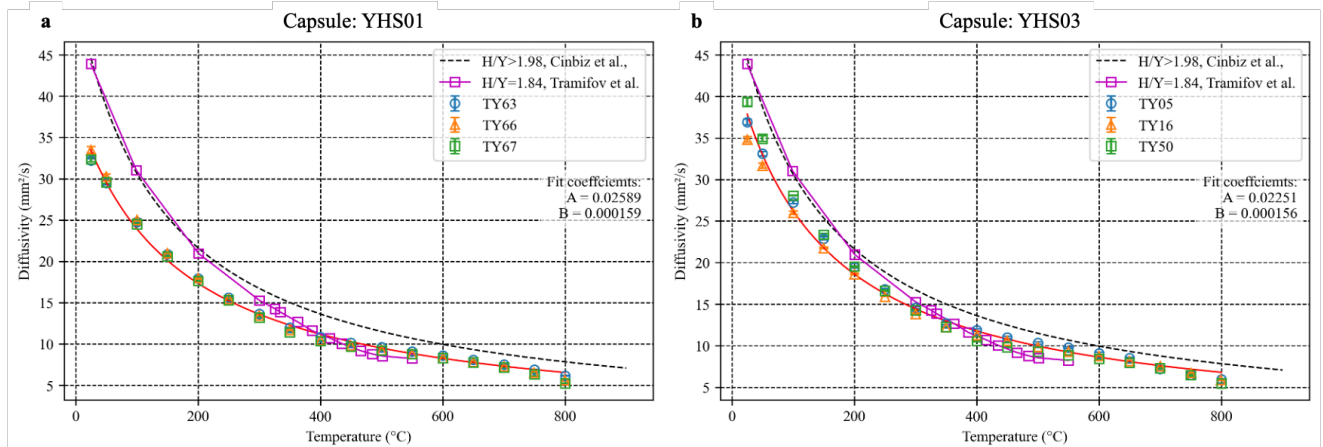


Figure 6-19 Capsule averaged thermal diffusivity (a) YHS01 and (b) YHS03

Table 6-4 presents the fitted parameters A and B for capsule-averaged thermal diffusivity of both HFIR and ATR-irradiated  $YH_x$  specimens under comparable experimental conditions. The parameter A, which captures the temperature-independent contribution to phonon scattering (primarily arising from static lattice defects, grain boundaries, second phase particles, and porosity), was consistently elevated in irradiated specimens relative to unirradiated (fresh)

references. This increase is attributed to irradiation-induced defect accumulation and potential hydrogen depletion, both of which enhance phonon scattering and reduce thermal transport capacity.

Among irradiated specimens, the A values for HFIR-irradiated samples were marginally higher than those from ATR, likely reflecting the difference in fast neutron fluence (and thus, displacement damage dose). Additionally, the time-at-temperature during irradiation may have influenced hydrogen redistribution and effusion kinetics, further modifying phonon scattering pathways through local stoichiometry and phase evolution.

The B parameter, representing the temperature-dependent scattering contribution predominantly due to Umklapp phonon-phonon interactions, exhibited no consistent trend across all irradiated specimens. However, the B values for HFIR-irradiated samples were slightly reduced relative to the ORNL fresh specimen (adapted from[22]). This reduction may be indicative of irradiation-induced structural disorder or alterations in short-range hydrogen ordering; both can suppress or modify the phonon scattering and shift the dominant scattering mechanisms.

Table 6-4 Capsule averaged thermal diffusivity of irradiated samples.<sup>1</sup>Calculation and <sup>2</sup>Measurement[10]

Specimen	Fabrication type	Reactor	Time (d)	Fast fluence #/cm <sup>2</sup> x10 <sup>21</sup> (E>0.1MeV)	T <sub>irr</sub> (°C)	A (s/mm <sup>2</sup> )	B (10 <sup>-4</sup> Ts/mm <sup>2</sup> )
YHS01	Direct	HFIR	22	2.7 <sup>1</sup>	532	0.0259	1.59
YHS03	Direct	HFIR	22	2.7	597	0.0225	1.56
LANL 600-4	Direct	ATR	60	1.3 <sup>2</sup>	610	0.0216	1.68
Fresh LANL (H/Y>1.98)	Direct	-	-	-	-	0.0190	1.36
Fresh ORNL (H/Y=1.84)	Direct	-	-	-	-	0.0180	1.67

## 6.6.2 DSC results

DSC measurements were performed to determine the specific heat capacity and investigate the transition temperature of second order transformation that is correlated to H/Y ratio. It has been shown that the transition temperature is correlated with the H/Y ratio. Figure 6-20 shows the specific heat capacity of specimen M013 (initial H/Y ratio = 1.83) that was subjected to HFIR-irradiation up to 0.1 dpa at 616°C. Specimen data was collected for 2 heating-cooling cycles to investigate the second-order transition behavior. The 1<sup>st</sup> cycle heating data indicated the transition occurred around ~409.8 °C. During cooling, the transition temperature increased to 434.3 °C, which can be considered a net increase in the H/Y of the YH<sub>x</sub> based on observations in [9, 10, 22]. For the 2<sup>nd</sup> heating cycle, the transition temperature was increased to 488.8 °C, indicating a further reduction of H/Y ratio, and the final whereas the transition temperature decreased to 465.3 °C, implying an increase in H/Y ratio.

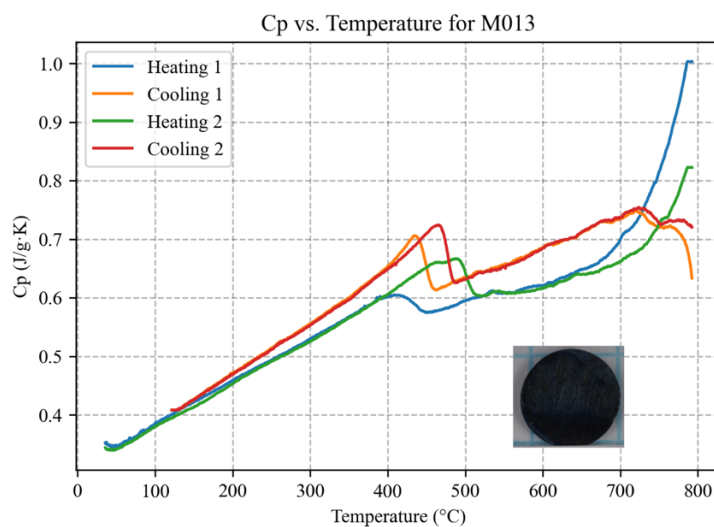


Figure 6-20 Specific heat capacity of specimen M013 (capsule YHXT07) for 2-cycle data collection. Initial H/Y ratio was 1.83,  $T_{irr} = 616$  °C, and 0.1 dpa. Inset shows the picture of the specimen.

DSC data of all other specimens are also shown in Figure 6-21, Figure 6-22, and Figure 6-23 for specimens from capsules YHS01, YHS03, YHX08, and YHX09, respectively.



## Capsule YHS01

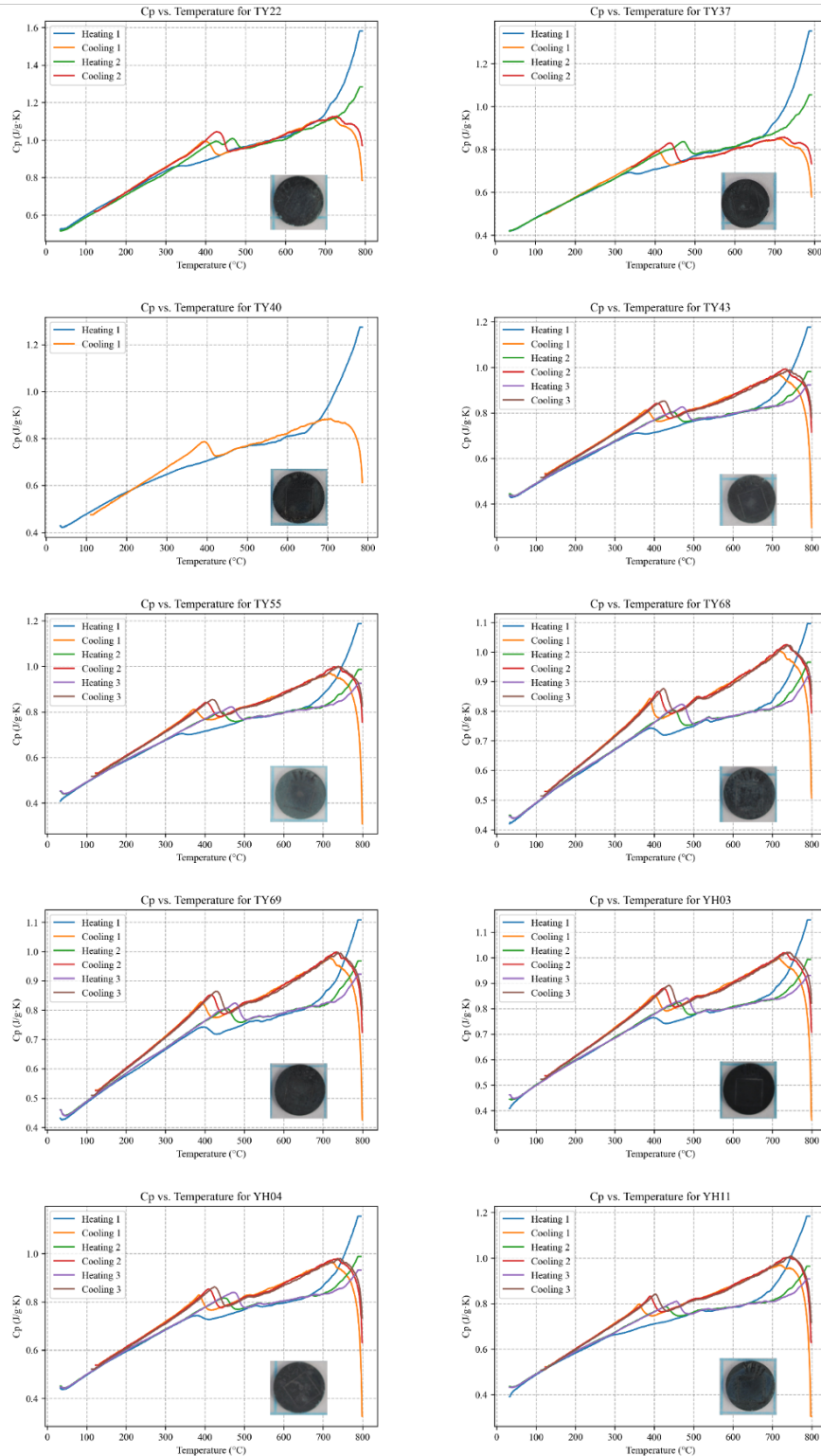


Figure 6-21 Specific heat capacity of specimens from the capsule YHS01. In total 10 specimens were tested for 1-3 cycles. Initial H/Y ratio was 1.87,  $T_{\text{irr}}=532^{\circ}\text{C}$ , and 2 dpa.

## Capsule YHS03

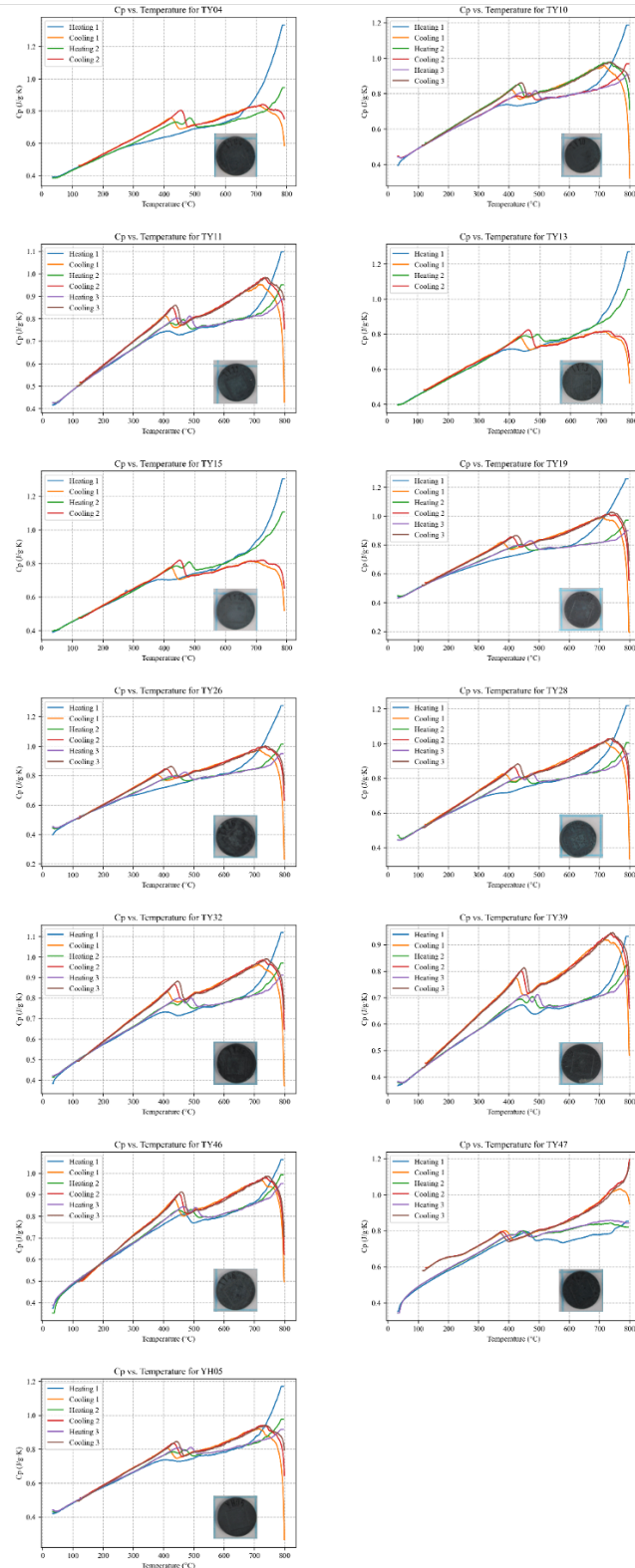


Figure 6-22 Specific heat capacity of specimens from the capsule YHS03. In total 13 specimens were tested for 1-3 cycles. Initial H/Y ratio was 1.87,  $T_{irr} = 597$  °C, and 2 dpa.

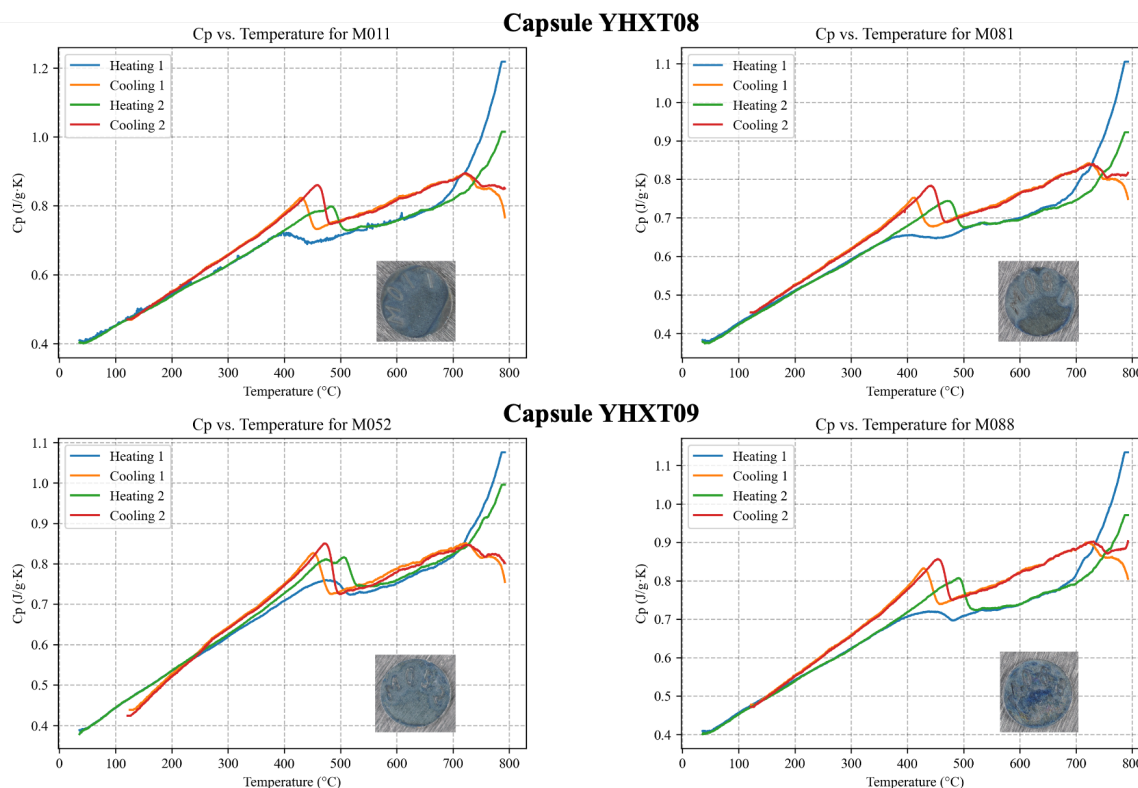


Figure 6-23 Specific heat capacity of specimens from the capsules YHX08 ( $T_{\text{irr}} = 640\text{ }^{\circ}\text{C}$ , 0.9 dpa) and YHX09 ( $T_{\text{irr}} = 532\text{ }^{\circ}\text{C}$ , 2 dpa). Per capsule, 2 specimens were tested. Initial H/Y ratio of all specimens was 1.83.

The specific heat of the irradiated specimens was determined using only the first cycle heating data to prevent potential hydrogen outgassing after the first cycle. The first cycle data were averaged for all specimens in the same capsule (see Figure 6-24). Because capsules YHS01 and YHS03 have a statistically meaningful number of tests, only the data from those capsules were fitted. Then, the average curve was fitted to a polynomial to determine the specific heat capacity. Like LFA data, the reported values were not absolute property measurements, but they are feasible to be used in nuclear fuel performance codes to meet engineering design goals.

Table 6-5 Fit coefficients for 6<sup>th</sup> degree polynomial for specific heat (only 1<sup>st</sup> heating cycle data used).

Mathematical form of the fit is:  $c_p(T) = aT^6 + bT^5 + cT^4 + dT^3 + eT^2 + fT + g$

Capsules	Range (°C)	a	b	c	d	e	f	g
YHS01	25-800	8.156	1.700	1.415	5.913	1.173	3.121	0.4215
		$10^{-17}$	$10^{-13}$	$10^{-10}$	$10^{-8}$	$10^{-5}$	$10^{-5}$	
YHS03	25-800	1.315	8.345	4.482	3.765	1.428	1.213	0.3617
		$10^{-17}$	$10^{-1-}$	$10^{-12}$	$10^{-9}$	$10^{-6}$	$10^{-3}$	

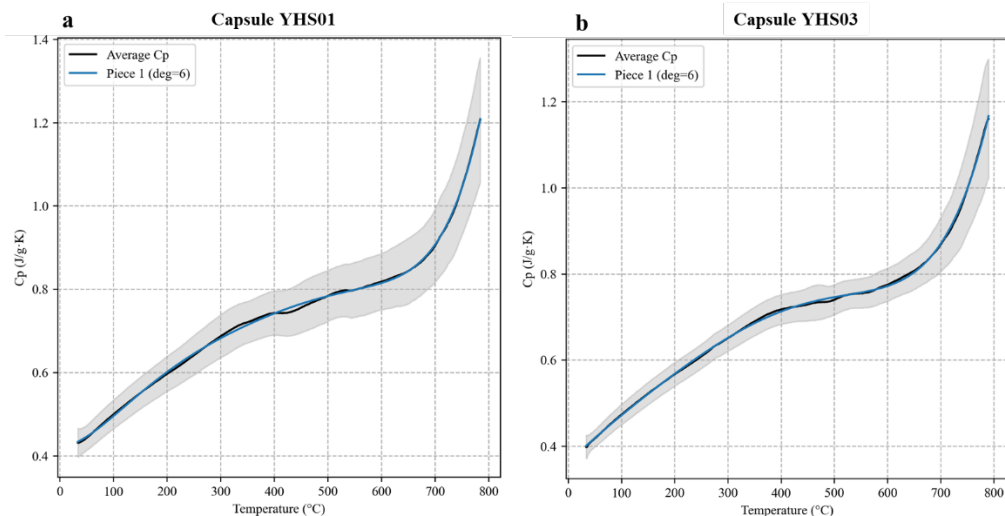


Figure 6-24 Capsule averaged specific heat (a) YHS01 and (b) YHS03. The gray shaded region shows the  $\pm 1\sigma$  bands

Irradiation damage in  $\text{YH}_x$  leads to the formation of vacancy/interstitial clusters and cavities. These defects can serve as sinks for H, allowing H atoms to migrate into or trapped at them. Additionally, hydrogen can outgas from the specimen into the surrounding environment. While outgassing results in irreversible hydrogen loss, hydrogen stored within defects—particularly cavities—can contribute to re-hydriding of the  $\text{YH}_x$  matrix, effectively increasing the measured H/Y ratio.

As a result, a net hydrogen loss is typically expected during DSC measurements over multiple thermal cycles, relative to the first DSC run. This trend holds unless the amount of hydrogen released from defects exceeds the amount lost through outgassing.

By analyzing changes in the transition temperature, a robust metric for hydrogen retention can be developed for the first cycle heating data. Alternatively, a decrease in transition temperature during the first cooling cycle—relative to the initial measurement—may indicate hydrogen release from defects. Recognizing these coupled phenomena, the heat capacity-based transition temperature can be considered a reliable and indirect metric for assessing hydrogen content in irradiated specimens.

In this report, our focal point was to determine the transition temperature for the first heating cycle to determine the H retention behavior after irradiation. The H/Y ratio was fitted with respect to transition temperature. A fifth order polynomial was fitted to the available data that related transition temperature to H/Y ratio using available data from [9, 22, 23]. The H/Y ratio (x) was approximately calculated as:

$$\text{H/Y} = 2.948 - 1.354 \times 10^{-2}T + 7.051 \times 10^{-5}T^2 - 1.846 \times 10^{-7}T^3 + 2.415 \times 10^{-10}T^4 - 1.278 \times 10^{-13}T^5$$

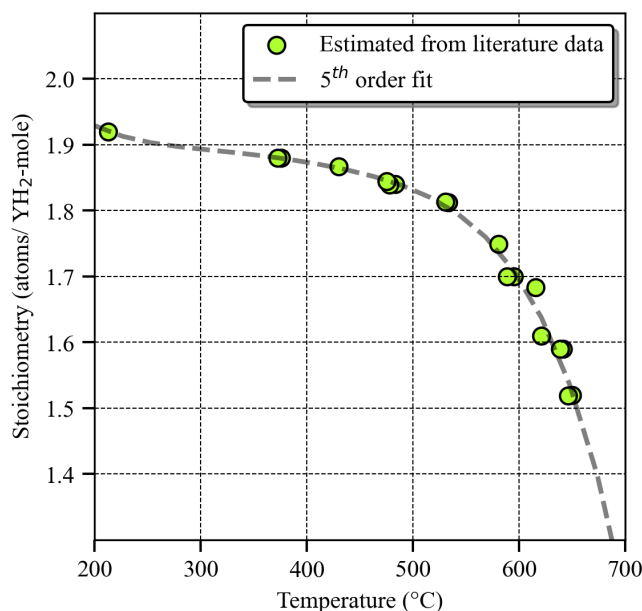


Figure 6-25 H/Y ratio versus transition temperatures, data is adapted and recalculated from [9, 22, 23]

Table 6-6 compares the initial and final H/Y ratios based on transition temperature calculations for the YHS01 and YHS03 specimens. The initial H/Y ratios were determined using mass measurements taken after fabrication. The average initial H/Y ratios for YHS01 and YHS03 were found to be 1.88 and 1.87, respectively.

In the YHS01 specimens, an increase in the H/Y ratio was observed after irradiation, indicating a rise in hydrogen content. This behavior may result from hydrogen being released from neighboring specimens and subsequently absorbed. However, it is important to note that initial H/Y ratios derived from mass measurements can carry significant uncertainty for small samples, as reported by Cinbiz et al. [24]. Therefore, the actual initial hydrogen loading in the specimens may have been higher than indicated by mass-based measurements.

Considering the known uncertainty in irradiation temperature measurements, a  $\pm 0.1$  variation in the H/Y ratio is within expected bounds. In the case of the YHS03 specimens, the overall H/Y ratio remained relatively constant, although some individual samples exhibited a slight decrease to 1.85. This suggests that while some specimens lost hydrogen, others absorbed it—likely during the cooldown phase following HFIR shutdown—maintaining the overall hydrogen content within the capsule.

It is worth noting that yttrium hydride exhibits strong hydrogen retention at irradiation temperatures, particularly due to its ability to trap hydrogen at irradiation-induced defects. Additionally, the presence of molybdenum provides extra shielding, which helps to minimize hydrogen loss.

Table 6-6 H/Y ratio evolution and transition temperatures for YHS01 and YHS03 specimens

Capsule	Specimen	dpa	Irradiation temperature (°C)	H/Y initial	Transition temperature (°C)	H/Y final
YHS01	TY22	2	532	1.87	335	1.89
YHS01	TY37	2	532	1.87	336	1.89
YHS01	TY40	2	532	1.87	300	1.89

YHS01	TY43	2	532	1.87	355	1.88
YHS01	TY55	2	532	1.87	341	1.89
YHS01	TY68	2	532	1.87	391	1.88
YHS01	TY69	2	532	1.87	397	1.87
YHS01	YH03	2	532	1.87	398	1.87
YHS01	YH04	2	532	1.87	377	1.88
YHS01	YH11	2	532	1.87	300	1.89
<b>Average</b>						<b>1.88</b>
YHS03	TY04	2	597	1.87	300	1.89
YHS03	TY13	2	597	1.87	412	1.87
YHS03	TY15	2	597	1.87	390	1.88
YHS03	TY19	2	597	1.87	300	1.89
YHS03	TY26	2	597	1.87	300	1.89
YHS03	TY28	2	597	1.87	300	1.89
YHS03	TY32	2	597	1.87	405	1.87
YHS03	TY39	2	597	1.87	440	1.86
YHS03	TY46	2	597	1.87	465	1.85
YHS03	TY47	2	597	1.87	457	1.86
YHS03	YH05	2	597	1.87	406	1.87
<b>Average</b>						<b>1.87</b>

## 7. KEY DISCUSSIONS

### 7.1 Effect of local varying hydride and metal phase fraction on the H retention

Post-irradiation cooling leads to spatially heterogeneous re-hydriding. Due to insufficient thermal energy, hydrogen diffusion is kinetically constrained, and thus, cannot homogenize across the specimen. This results in local variations in the phase fraction – observed in the relative intensity changes of  $\delta$ -YH<sub>2</sub> and  $\alpha$ -Y peaks and broadened peaks. Although XRD data cannot resolve hydrogen content at the atomic level, changes in the diffraction peak intensities support the hypothesis of localized loss of hydrogen as a result neutron irradiation.

To better understand the local phenomenon of hydrogen redistribution and eventual loss, diffraction spectra were collected using micro-focused X-ray beam in a single-point spot mode from different localized regions within the same specimen having similar irradiation history as the specimens in capsules YHS01 and YHS03. As can be seen in Figure 7-1, there is a change in the relative intensities of the major diffraction peaks for each sampling location. However, the hydride-metal peak intensity ratios, though non-uniform, do not vary significantly within the probed volumes.

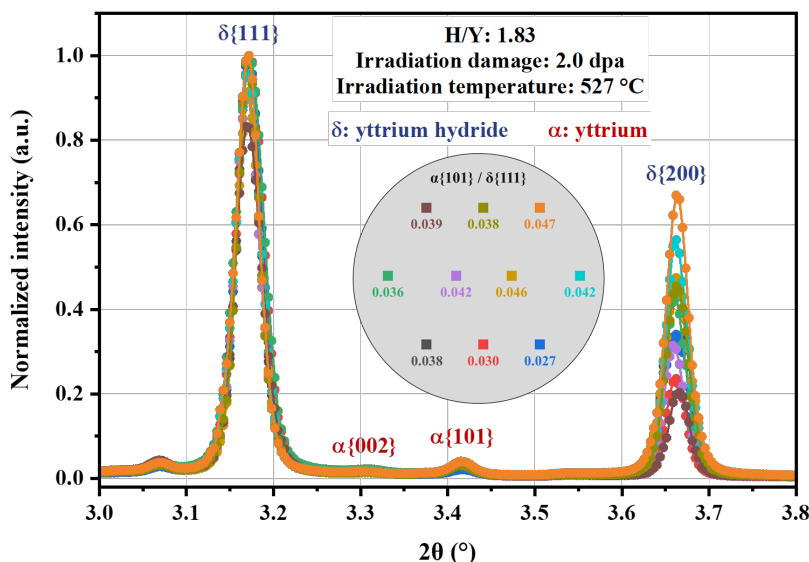


Figure 7-1 Experimental XRD spectra obtained from different sampling locations within the same sample which has similar irradiation history as the specimens in capsules YHS01 and YHS03. The inset shows a schematic representation of the irradiated  $\text{YH}_x$  disc, with different colored boxes representing the different probed volumes. The corresponding spectra obtained from each of these probed volumes are shown in the same color. The intensity ratio variations of  $\{101\}$  diffraction peak of  $\alpha$ -Y and  $\{111\}$   $\delta$ - $\text{YH}_2$  peak are indicated in the inset.

Overall,  $\text{YH}_x$  exhibits extraordinary structural and phase stability under neutron irradiation conditions.

## 7.2 Hydride stability under irradiation

Hydrogen retention behavior in sub-stoichiometric yttrium hydrides is critically influenced by neutron irradiation conditions and post-irradiation thermal histories. During HFIR irradiation, elevated temperatures promote hydrogen release from the  $\text{YH}_x$  matrix, leading to an increase in the hydrogen partial pressure within the capsule environment. However, post irradiation, the specimens undergo cooling— the released hydrogen must either recombine with the matrix or be trapped in available defect structures, such as the cavities.

Synchrotron XRD in the transmission mode provides a non-destructive and quantitative method to assess the resulting phase fraction in the bulk specimen. As can be seen in the XRD spectra obtained from the irradiated specimens, the hydride peaks are very prominent whereas the  $\{101\}$  peak associated with  $\alpha$ -Y phase were too weak and broad. This can be attributed to the presence of fewer crystalline planes of metallic yttrium in the sample, suggesting significant hydrogen retention. The presence of nanocavities, as confirmed by TEM analyses, aids the interpretation of experimental results. While XRD cannot detect the hydrogen trapped within these voids, their role as transient hydrogen sinks is significant. These trapped hydrogen atoms may later re-precipitate locally, thereby, enhancing the spatial inhomogeneity of the hydride phase. Moreover, re-hydriding phenomenon inferred from XRD patterns – such as suppression of metallic  $\alpha$ -Y peaks after irradiation – indicates that the trapped hydrogen within the specimen is mobile and there exists a dynamic equilibrium between the hydrogen in the lattice and that in nanocavities.



### 7.3 Microstructure and H retention

The microstructure of neutron-irradiated  $\text{YH}_x$  is characterized by the formation of interstitial/vacancy defect clusters and cavities. In addition to these irradiation-induced defects, an amorphous layer was observed at the periphery of the hydrides, along with an interfacial oxide layer between the amorphous region and the hydride matrix. As shown in Figure 7-2, the thickness of the amorphous layer decreases with increasing irradiation dose, while the oxide layer at the interface becomes more continuous.

These microstructural features are expected to enhance hydrogen (H) retention during operation. The amorphous layer primarily consists of an oxygen-rich compound, likely an oxide. The presence of such an O-rich amorphous layer can improve hydrogen retention performance, as high hydrogen permeation reduction factors (PRFs) have been reported for yttria coatings [25, 26] and oxides in general [25-32]. This formed barrier is expected to suppress hydrogen egress during reactor operation. Furthermore, the continuous nature of the oxide layer with increasing dose suggests a potential for enhanced long-term hydrogen retention, particularly under extended irradiation conditions.

Additionally, the presence of irradiation-induced cavities may contribute to increased H retention by serving as hydrogen storage pockets during operation. A similar effect is expected from defect clusters, which can locally trap hydrogen. Overall, irradiation damage is anticipated to enhance hydrogen retention throughout the reactor's operational lifetime.

Transition temperature-based assessments of the H/Y ratio revealed no measurable hydrogen loss during the initial heating cycle post-irradiation, indicating that the majority of hydrogen remained sequestered within the  $\text{YH}_x$  phase. Moreover, hydrogen accommodated in cavities during operation is expected to be reabsorbed by the surrounding  $\text{YH}_x$  matrix once HFIR irradiation ceases.

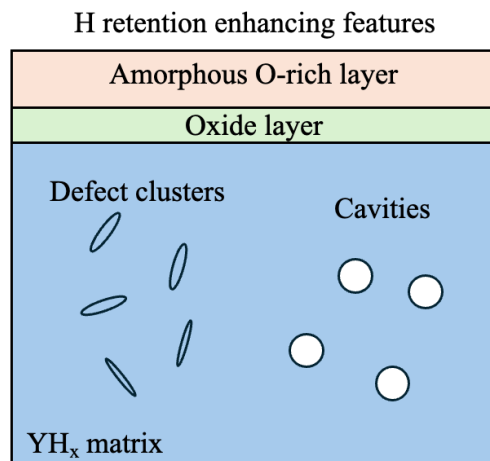


Figure 7-2 Illustration of H retention enhancing features in irradiated  $\text{YH}_x$

### 7.4 Importance of an accurate hydrogen retention metric for irradiated specimens

Quantifying H retention is critical for evaluating the irradiation performance of hydride moderators. In prototypical or full-scale components consisting of yttrium and cladding materials,



the relative mass contribution of H is minimal. As a result, conventional mass measurements lack the resolution necessary to detect hydrogen loss or retention with sufficient accuracy. Therefore, robust and representative methods are essential to assess irradiation performance of hydride moderators.

Direct analytical techniques for H quantification, such as thermal desorption spectroscopy or carrier gas hot extraction, can be employed; however, they typically require small sample volumes, which may not accurately reflect bulk moderator behavior. As an alternative, thermal property measurements provide a valuable indirect method. Specifically, the observed order-disorder transition temperature is strongly correlated with the H/Y atomic ratio. This transition can be captured via differential scanning calorimetry (DSC), as demonstrated in this post-irradiation examination (PIE) campaign.

Additionally, thermal expansion measurements offer a complementary approach, wherein the transition behavior is similarly detectable and allows for the use of larger specimens. This enables evaluation of more representative test articles and supports technological readiness level (TRL) advancement. Conversely, high-resolution techniques such as DSC or transmission-mode XRD are well-suited for examining hydrogen behavior in small-scale samples, which is particularly useful for hydride and cladding alloy development in microreactor applications.

## 8. CONCLUSIONS AND SUGGESTED FUTURE WORK

ORNL have conducted PIE on HFIR irradiated  $\text{YH}_x$  specimens from the second HFIR irradiation campaign and carefully selected specimens from the first campaign. PIE activities focused on the determination of thermal properties and H retention behavior in the specimens. H retention was evaluated through electron microscopy, XRD, and heat capacity measurements. The dissimilar materials compatibility was also investigated by examining H retention.

Key conclusions of the ORNL PIE are:

- **Structural stability and H retention:** Yttrium hydrides demonstrated high structural stability and excellent hydrogen retention under the applied HFIR irradiation conditions.
- **Surface interactions with dissimilar materials:** Surface discoloration indicated that the hydride reacted with stainless steel and SiC at contact interfaces. However, these interactions did not adversely affect hydrogen retention under the given conditions.
- **Microstructural effects:** Microstructural characterization suggested that enhanced hydrogen retention was primarily driven by irradiation-induced defect formation and interface modification through irradiation-enhanced diffusion and transformation processes.
- **Thermal diffusivity behavior:** Irradiated specimens exhibited increased phonon scattering and reduced thermal diffusivity, as reflected by higher A values in the  $1/(A + BT)$  trend. Slightly lower B values in HFIR specimens suggested structural disorder or hydrogen redistribution affecting phonon interactions.
- **Heat capacity as a retention metric:** Heat capacity measurements were used to determine the order-disorder transition temperature, providing a reliable estimate of the post-irradiation H/Y ratio. This approach offered a robust metric for assessing hydrogen retention.

- **Phase non-uniformity:** High-energy XRD revealed that the YH<sub>x</sub> phase fraction varied across the specimen's radial position, indicating non-uniform re-hydriding during reactor cool-down. This variation was likely influenced by localized hydriding near irradiation-induced defects.

Based on PIE observations from ATR and HFIR irradiated specimens, our recommendations for future work:

- **Alloy development:** Leverage insights from this and previous INL PIE studies to develop improved yttrium-based hydride alloys with enhanced hydrogen retention.
- **Prototypic irradiation testing:** As the ATR and ORNL irradiations were performed on small specimens, future efforts should focus on irradiating full-scale moderator elements to assess hydride and cladding performance at end-of-life doses. HFIR presents a unique testbed for such prototypic irradiation experiments and supports timely technology deployment.
- **Science-driven exploration:** Integrate computational and experimental studies to explore novel moderator materials and identify new opportunities for hydride development.

In summary, the completion of ORNL's PIE marks a significant step toward the development of advanced hydride alloys and supports the deployment of hydride-based moderators in microreactors. The recommended future activities will further enhance technology readiness and also benefit the development of novel nuclear components.

## 9. REFERENCES

- [1] A microreactor program plan for the Department of Energy INL/EXT-20-58191, Idaho National Laboratory, Idaho Falls, 2020, p. 23.
- [2] M.N. Cinbiz, PLN-6268 Yttrium Hydride Post Irradiation Examination Plan, United States, 2022, p. Medium: ED.
- [3] J.B. Vetrano, Hydrides as neutron moderator and reflector materials, *Nuclear Engineering and Design* 14(3) (1971) 390-412.
- [4] W.M. Mueller, Chapter 2 - Hydrides in Nuclear Reactor Applications, in: W.M. Mueller, J.P. Blackledge, G.G. Libowitz (Eds.), *Metal Hydrides*, Academic Press 1968, pp. 21-50.
- [5] M.N. Cinbiz, C.N. Taylor, E. Luther, H. Trellue, J. Jackson, Considerations for Hydride Moderator Readiness in Microreactors, *Nuclear Technology* (2022) 1-10.
- [6] P. Champlin, J. Burns, C.M. Petrie, X. Hu, K.D. Linton, R.H. Howard, K.A. Terrani, Capsule and Specimen Geometries for HFIR Irradiation Testing Supporting the Transformational Challenge Reactor, United States, 2019.
- [7] A. Le Coq, K.D. Linton, P.A. Champlin, R. Howard, T.S. Byun, K.A. Terrani, HFIR Irradiation Testing Supporting the Transformational Challenge Reactor, Oak Ridge National Laboratory, Oak Ridge, 2020.
- [8] M.N. Cinbiz, J.A. Charboneau, I.M. Hobbs, G.C. Papaioannou, T.A. Johnson, L.A. Hone, S.C. Middlemas, C.N. Taylor, Initial Post Irradiation Examination of Irradiated Yttrium Hydride, (2022).
- [9] M.N. Cinbiz, C.N. Taylor, T. Johnson, J.A. Charboneau, I.M. Hobbs, S.C. Middlemas, N. Poudel, T.R. Pavlov, G.C. Papaioannou, L.A. Hone, Post Irradiation Examination Results of Irradiated Yttrium Hydride, Idaho National Laboratory (INL), Idaho Falls, ID (United States), 2023.
- [10] M.N. Cinbiz, C.N. Taylor, T.A. Johnson, J.A. Charboneau, I.M. Hobbs, J. Burns, S.C. Middlemas, N. Poudel, T.R. Pavlov, G.C. Papaioannou, Report on the Incorporation of Post-Irradiation Examination

Results of Yttrium Hydride for Advanced Moderator Handbook, Idaho National Laboratory (INL), Idaho Falls, ID (United States), 2023.

- [11] A.P. Shivprasad, M.N. Cinbiz, J.R. Torres, T.E. Cutler, D. Wootan, J.K. Jewell, V.K. Mehta, S. Widgeon Paisner, C.A. Kohnert, C. Taylor, Advanced Moderator Material Handbook (FY23 Version), Los Alamos National Laboratory (LANL), Los Alamos, NM (United States), 2023.
- [12] A.G. Le Coq, T.G. Lach, W. Zhong, D. Sprouster, K.D. Linton, P.A. Champlin, T. Koyanagi, M. Nedim Cinbiz, Phase stability and microstructure of neutron-irradiated substoichiometric yttrium dihydrides, *Journal of Nuclear Materials* 603 (2025).
- [13] M. Nedim Cinbiz, T. Lach, M. Topsakal, A. Le Coq, K. Linton, Impact of nano-scale cavities on hydrogen storage and retention in yttrium hydride, *Materialia* 32 (2023).
- [14] P.A. Champlin, C.M. Petrie, A.G. Le Coq, K.R. Smith, K.D. Linton, Thermal Analysis and Irradiation Growth of Coated Zirconium Alloy Cladding Specimens in HFIR (ORNL/TM-2020/1567), Oak Ridge National Laboratory, Oak Ridge, TN (United States). 2020.
- [15] Differential scanning calorimeter use for temperature monitor analysis (MST-LAMDA-SOG-015), Oak Ridge National Laboratory, Oak Ridge, 2025.
- [16] K.G. Field, J.L. McDuffee, J.W. Geringer, C.M. Petrie, Y. Katoh, Evaluation of the continuous dilatometer method of silicon carbide thermometry for passive irradiation temperature determination, *Nuclear Instruments and Methods in Physics Research Section B: Beam Interactions with Materials and Atoms* 445 (2019) 46-56.
- [17] A.A. Campbell, W.D. Porter, Y. Katoh, L.L. Snead, Method for analyzing passive silicon carbide thermometry with a continuous dilatometer to determine irradiation temperature, *Nuclear Instruments and Methods in Physics Research Section B: Beam Interactions with Materials and Atoms* 370 (2016) 49-58.
- [18] A. International, Standard Test Method for Thermal Diffusivity by the Flash Method (ASTM E1461-13), West Conshohocken, PA, 2022.
- [19] Thermal diffusivity testing standard operating guideline - LFA467 (MST-LAMDA-SOG-013), Oak Ridge National Laboratory, Oak Ridge, 2024.
- [20] ASTM International, Standard Test Method for Enthalpies of Fusion and Crystallization by Differential Scanning Calorimetry (ASTM E793-24), West Conshohocken, PA, 2024.
- [21] Differential scanning calorimeter standard operating guideline (MST-LAMDA-SOG-006), Oak Ridge National Laboratory Oak Ridge, TN, 2024.
- [22] A.A. Trofimov, X. Hu, H. Wang, Y. Yang, K.A. Terrani, Thermophysical properties and reversible phase transitions in yttrium hydride, *Journal of Nuclear Materials* 542 (2020).
- [23] A.P. Shivprasad, S.C. Vogel, V.K. Mehta, M.W.D. Cooper, T.A. Saleh, J.T. White, J.R. Wermer, E.P. Luther, H.R. Trellue, Thermophysical properties of high-density, sintered monoliths of yttrium dihydride in the range 373–773 K, *Journal of Alloys and Compounds* 850 (2021).
- [24] M.N. Cinbiz, J.A. Charboneau, I.M. Hobbs, T.A. Johnson, C.N. Taylor, Report On Hydrogen Content Measurements of Yttrium Hydrides, Idaho National Laboratory (INL), Idaho Falls, ID (United States), 2023.
- [25] J. Engels, A. Houben, C. Linsmeier, Hydrogen isotope permeation through yttria coatings on Eurofer in the diffusion limited regime, *International Journal of Hydrogen Energy* 46(24) (2021) 13142-13149.
- [26] J. Engels, A. Houben, P. Hansen, M. Rasinski, C. Linsmeier, Influence of the grain structure of yttria thin films on the hydrogen isotope permeation, *International Journal of Hydrogen Energy* 43(51) (2018) 22976-22985.
- [27] X. Xiang, X. Wang, G. Zhang, T. Tang, X. Lai, Preparation technique and alloying effect of aluminide coatings as tritium permeation barriers: A review, *International Journal of Hydrogen Energy* 40(9) (2015) 3697-3707.
- [28] A. Sundar, J. Yu, L. Qi, M. Nedim Cinbiz, High temperature stability and transport characteristics of hydrogen in alumina via multiscale computation, *International Journal of Hydrogen Energy* (2022).
- [29] V. Somjit, B. Yildiz, Doping  $\alpha$ -Al<sub>2</sub>O<sub>3</sub> to reduce its hydrogen permeability: Thermodynamic assessment of hydrogen defects and solubility from first principles, *Acta Materialia* 169 (2019) 172-183.

- [30] A. Perujo, K.S. Forcey, Tritium permeation barriers for fusion technology, *Fusion Engineering and Design* 28 (1995) 252-257.
- [31] V. Nemanič, Hydrogen permeation barriers: Basic requirements, materials selection, deposition methods, and quality evaluation, *Nuclear Materials and Energy* 19 (2019) 451-457.
- [32] G.W. Hollenberg, E.P. Simonen, G. Kalinin, A. Terlain, Tritium/hydrogen barrier development, *Fusion Engineering and Design* 28 (1995) 190-208.